Journal of Electron Spectroscopy and Related Phenomena 200 (2015) 293–310

Contents lists available at ScienceDirect

Journal of Electron Spectroscopy and Related Phenomena

journal homepage: www.elsevier.com/locate/elspec

Development and application of *in situ*/*operando* soft X-ray transmission cells to aqueous solutions and catalytic and electrochemical reactions

Masanari Nagasaka[a,b], Hayato Yuzawa[a], Nobuhiro Kosugi[a,b,*]

[a] *Institute for Molecular Science, Myodaiji, Okazaki 444-8585, Japan*
[b] *SOKENDAI (Graduate University for Advanced Studies), Myodaiji, Okazaki 444-8585, Japan*

ARTICLE INFO

Article history:
Available online 5 June 2015

Keywords:
In situ soft X-ray absorption spectroscopy
Aqueous solution
In operando XAFS
Catalytic reaction
Electrochemical reaction

ABSTRACT

In this review, we have demonstrated several applications of newly-developed *in situ*/*operando* liquid flow cells for the transmission XAS (X-ray absorption spectroscopy) measurement in the soft X-ray undulator beamline BL3U dedicated to the chemical application of UVSOR-III Synchrotron. The liquid layer is sandwiched between two thin membranes and its thickness is easily controllable to optimize the absorbance. Liquid samples are exchangeable *in situ*. Molecular spectra in liquid and gas phases are simultaneously measureable and it makes the energy calibration rather easy. By using a standard version of the liquid cells, we have investigated local structures of several aqueous solutions of alkali halides, methanol, pyridine, and acetonitrile. To observe catalytic and electrochemical reactions under realistic conditions, we have developed *in situ*/*operando* versions of the liquid cells. We have investigated local structures of the catalytic hydration reaction of cyanopyrazine under the temperature control and the electrochemical reaction of aqueous iron sulfate solutions using the built-in electrodes under the same scan rate as in cyclic voltammetry. We have discussed future perspectives of our *in situ*/*operando* liquid flow cells applied to XAS in the soft X-ray region.

1. Introduction

Macroscopic properties of aqueous solutions, such as viscosity, boiling point, and freezing point, are determined by the interaction between solvent water molecules and solute ions or molecules. In aqueous salt solutions, hydrogen bonding (HB) networks of water molecules are modified or broken by the interactions with solute ions [1–3]. In aqueous methanol solutions, the entropy is smaller than expected in an ideal solution of randomly mixed molecules [4] and shows a nonlinear profile in viscosity at different concentrations [5], indicating some structured interactions between water and methanol molecules. The bond lengths and the coordination numbers of solute ions and molecules with solvent water molecules in aqueous solutions have been extensively studied by neutron diffraction [6–8] and X-ray diffraction [9].

In addition, spectroscopic studies are crucial to reveal the interaction between solvent water molecules and solute ions or molecules: for example, vibrational spectroscopies such as infrared (IR) and Raman spectroscopies. For example, the OH stretching mode is effectively observed in Raman spectroscopy [10–12] to reveal the hydration structure of the anion to the hydrogen of water in aqueous salt solutions. In aqueous pyridine solutions, the HB interaction between N atoms in pyridine and water molecules is revealed by IR [13] and Raman spectroscopy [14,15]; in aqueous acetonitrile solutions, the HB interaction is revealed by the C≡N and OH stretching modes in IR spectroscopy [9,16,17]. In aqueous methanol solutions, the local structures around methanol molecules at different concentrations are revealed by the C—O stretching modes in Raman spectroscopy [18]. However, vibrational spectroscopy is not enough to understand the local molecular interaction in solutions. For example, the OH stretching mode is not so useful to reveal the hydration structure of the cation to the oxygen of water. Minor components are often hindered by dominant vibrations of solvent molecules with similar wavenumbers. Therefore, the interaction of solutes with solvent water molecules in aqueous solutions should be investigated by combination with other spectroscopies sensitive to the local molecular interaction.

X-ray absorption spectroscopy (XAS) is an element-specific method to study local structures of aqueous solutions. Especially, the soft X-ray region below 1 keV has chemically important

* Corresponding author at: SOKENDAI (Graduate University for Advanced Studies), Institute for Molecular Science, Myodaiji, Okazaki 444-8585, Japan. Tel.: +81 564 55 7390; fax: +81 564 54 7079.
E-mail address: kosugi@ims.ac.jp (N. Kosugi).

http://dx.doi.org/10.1016/j.elspec.2015.05.012
0368-2048/

absorption edges such as C K-edge (280 eV), N K-edge (400 eV), and O K-edge (530 eV). Observation of the L-edge (2p) spectra of 3d transition metals such as Ti L_{III}-edge (460 eV) and Cu L_{III}-edge (930 eV) is important, considering that the L-edge of 3d transition metals is more sensitive than the K-edge to the 3d valence and spin states [19–21]. Recently, the local structures of liquid water have been extensively studied by O K-edge XAS [22–34], where the pre-edge peak (535 eV) corresponds to the transition from the O 1s electron to the '$4a_1$' unoccupied state, and the behavior of the pre-edge '$4a_1$' peak reflects the HB interaction effect on a molecular $4a_1$ orbital. The temperature dependence of the pre-edge peak is observed to reveal the change in local structure of the HB network in liquid water [25,26,29,31,33,34]. The pre-edge peak in O K-edge XAS of aqueous salt solutions is sensitive to the hydration structure of solute ions (especially, cations) [35–42]. On the other hand, the C and N K-edge XAS can be used to reveal the local structure of solute molecules in aqueous solutions. For example, in aqueous methanol solutions, the hydrophobic interaction of the methyl group in methanol molecule is revealed in the C K-edge XAS [43–45].

XAS is a quite promising method to investigate the local structure of aqueous solutions. XAS spectra of liquid samples can be obtained in transmission mode [30,32–34,46] based on the Lambert–Beer law. XAS-like spectra are measured by fluorescence yields [23,24,26,28], hard X-ray Raman scattering [22,29,31], and total electron yields [25] and inverse partial fluorescence yields [47–49] of microjet liquids. In these alternative methods, comparison with the transmission spectra is discussed as regards background subtraction, normalization, saturation effect, and self-absorption effect, and indicates that XAS-like spectra of bulk liquids measured by hard X-ray Raman scattering and by inverse partial fluorescence yields is nearly the same as XAS spectra in transmission mode. Combination with theoretical simulations of the O K-edge XAS of liquid water is important in revealing its local structure [23,24,26,28,50–56], but should be compared with the true transmission spectrum based on the Lambert–Beer law in the case of quantitative and detailed discussion of spectral features in XAS. However, it is difficult to measure XAS spectra of liquid samples in transmission mode because soft X-rays are strongly absorbed by solvent water beyond the water window region and the thickness of the liquid layer should be kept below a few micrometers [57].

Recently, we have successfully developed some unique liquid flow cells for XAS of liquid samples in transmission mode [30]. The cell is attachable to our IR spectrometer as it is. By using a standard version of liquid flow cells, we have investigated the local structures of several aqueous solutions, such as aqueous salt [42], methanol [45], pyridine [58], and acetonitrile solutions [59]. Furthermore, we have developed *in situ*/*operando* XAS observation systems to measure the local structural change in catalytic and electrochemical reactions under realistic conditions by extending our liquid cell approach. We have investigated cyanopyrazine (PzCN) hydration reaction to produce pyrazinamide ($PzCONH_2$) on the TiO_2 catalyst [60] and the change in valence of Fe ions in aqueous iron sulfate solutions from the Fe L-edge XAS spectra [61,62]. In the present review, we describe details of our liquid flow cells for the transmission XAS measurement and several applications to aqueous solutions and catalytic reactions in Section 2 and to electrochemical reactions in Section 3. In Section 4, we summarize the present applications and discuss the future perspectives.

2. Aqueous solutions and catalytic reactions

2.1. In situ *liquid flow cell*

Fig. 1 shows schematics of the liquid flow cell for XAS in transmission mode [30]. The cell consists of four regions (I), (II), (III), and (IV), separated by 100 nm-thick Si_3N_4 membranes. The Si_3N_4 membrane cannot be used for the N K-edge measurement, but the SiC membrane can be used. Region (I) is connected to the beamline under vacuum. Regions (II) and (IV) are under atmospheric pressure of helium pure gas or mixed gas with reference or other molecules. The size of the Si_3N_4 (SiC) membrane window between regions (I) and (II) is 0.2 mm × 0.2 mm, which is small enough to endure a large difference in pressure, even larger than 1 atm. This orifice determines the size of the soft X-ray beam on the sample. The flow rate of the helium gas in regions (II) and (IV) is changeable by a mass flow controller, and the pressure is adjusted by a needle valve at the gas outlet of regions (II) and (IV).

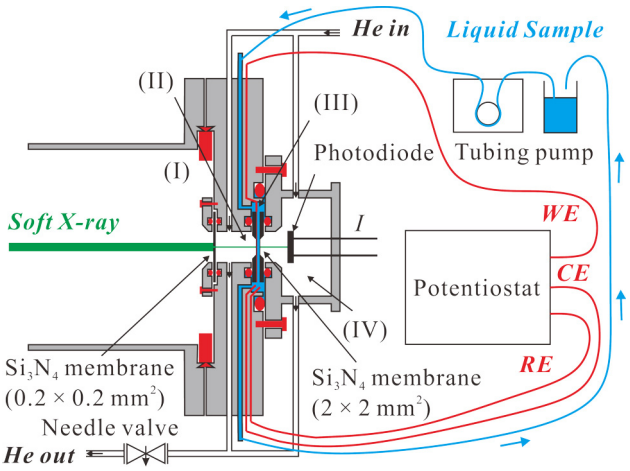

Fig. 1. Schematic of a simple version of the liquid flow cells for XAS in transmission mode [30]. The details of the cell are described in the text. The electrochemical cell will be shown later (Fig. 22). Any liquid flow cell developed in the present work is attachable as it is to IR spectrometers as well as soft X-ray beamlines.

The thin liquid layer in region (III) is sandwiched between two 100 nm-thick Si_3N_4 membranes with a window size of 2 mm × 2 mm. The liquid flow is under atmospheric condition. Two 100 μm-thick spacers are set between the window frames of the membranes and the frames are compressed by the sealing O-rings to keep the thin liquid layer between the membrane windows below 2000 nm. Liquid samples can be exchanged *in situ* with a tubing pumping system. The temperature of the liquid flow cell can be changed from −5 °C to 75 °C. The thickness of the liquid layer is controllable between 20 nm and 2000 nm by changing the He pressure in regions (II) and (IV).

In order to measure XAS spectra of liquid samples, soft X-rays pass through regions (I), (II), and (III) and are detected by a photodiode in region (IV). The intensity of soft X-rays is normalized by an electric current of a gold mesh in region (I), where the current is proportional to the photon flux. The absorption of soft X-rays in regions (II) and (IV) is small due to the high transmittance of helium [57].

The experiments were performed on the soft X-ray in-vacuum undulator beamline BL3U at UVSOR-III Synchrotron [63]. The XAS spectra are obtained by using the Lambert–Beer formula $\ln(I_0/I)$, in which the transmission signal intensity I_0 is measured for the blank and the transmission signal intensity I is for the liquid sample. The photon energy is calibrated by using the first peak (287.96 eV) of methanol gas [44], the first peak of N 1s → π* band (400.84 eV) of N_2 gas [64], and the O 1s → π* peak top (530.80 eV) of O_2 gas [65], which are mixed with helium gas in regions (II) and (IV).

Fig. 2 shows O K-edge XAS spectra of liquid water at different thicknesses. As shown in the inset of Fig. 2, the thickness of the liquid layer is successfully controlled by adjusting the pressure of the helium buffer gas in regions (II) and (IV). Note that it does not show correct absorption spectra because we did not use energy

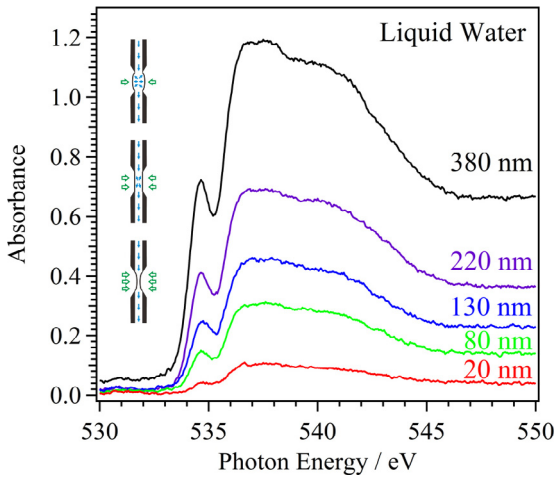

Fig. 2. O K-edge XAS spectra of liquid water at different thickness. The inset shows the schematics of the thin liquid layer, in which the thickness is controllable between 20 nm and 2000 nm by adjusting the helium pressure. Note that higher order photons are included here but are cut by using energy filters in the other spectra shown in this review.

filters to cut higher-order soft X-rays from the BL3U monochromator or did not optimize the sample position with uniform thickness in the sample area absorbing soft X-rays when we measured them [30]. Other spectra shown in this review were measured by using the energy filters. The thickness T [nm] of the liquid layer can be estimated from the edge jump μT of the measured XAS spectrum and the absorption coefficient μ [nm^{-1}] of liquid water obtained in Ref. [57].

2.2. Alkali halide solution

The hydration structures of ions in aqueous salt solutions were extensively studied by neutron diffraction [6,8,66–69], X-ray scattering [70–73], extended X-ray absorption fine structure spectroscopy [74], and X-ray diffraction [75]. The electronic structures of hydration shells in aqueous salt solutions were studied by photoelectron spectroscopy [76] and X-ray emission spectroscopy [77]. Molecular dynamics (MD) simulations were carried out for the hydration structures of cations in aqueous salt solutions [78–91]. Cations are coordinated with oxygen atoms in water molecules, and anions are coordinated with hydrogen atoms in water molecules.

Na K-edge XAS revealed that both Na^+ and Cl^- ions are coordinated with the same water molecule in highly concentrated NaCl solutions [92]. The solvent-shared ion pair is also confirmed in LiCl solutions by dielectric relaxation measurement [93]. The interactions of anions with water molecules were extensively studied by using the OH stretching mode in Raman spectroscopy [10–12]. The hydration shell of anions is reconstructed within several pico seconds, as observed by time-resolved IR and Raman spectroscopy [94–97]. On the other hand, the hydration shell of cations has not yet been studied in detail.

Recently, several groups have measured the O K-edge XAS spectra of aqueous salt solutions, and discussed the hydration structures of cations from the energy shift of the '$4a_1$' pre-edge peak [35–41]. The $4a_1$ orbital is mainly distributed at the oxygen atom in the water molecule, and therefore the energy shift of the pre-edge peak would reflect the interaction of the cation with water molecule. However, the O K-edge XAS spectra of aqueous salt solutions, measured by different detection methods, show different results and conflicting interpretations on the energy shift of the pre-edge peak [35–41].

The temperature dependent change of the O K-edge XAS spectra is important in investigation of the hydration structure of cations in

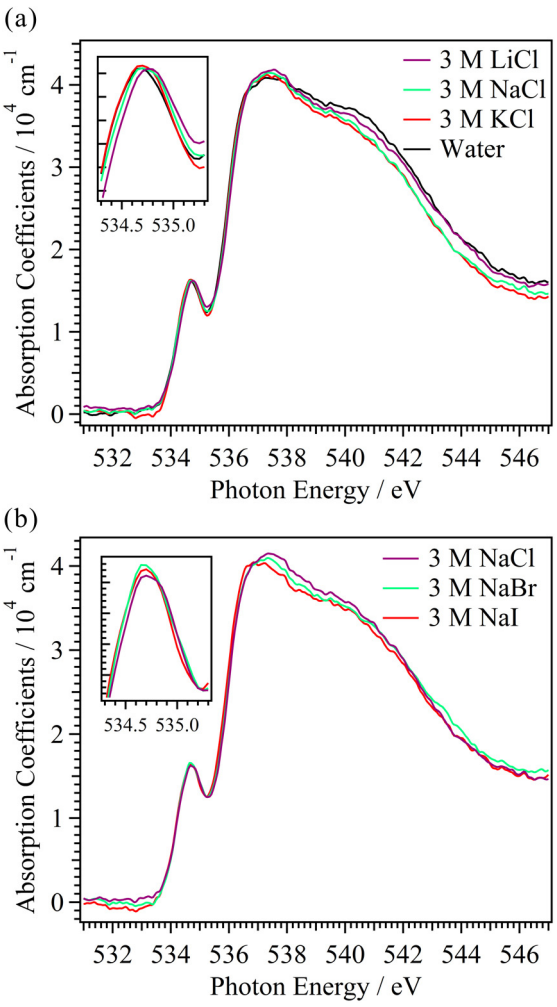

Fig. 3. (a) O K-edge XAS spectra of liquid water and aqueous salt solutions with different cations (3 M LiCl, 3 M NaCl, and 3 M KCl) at 25 °C. (b) O K-edge XAS spectra of aqueous salt solutions with different anions (3 M NaCl, 3 M NaBr, and 3 M NaI) at 25 °C. The inset shows the expansion of the pre-edge region.

aqueous salt solutions. Several groups have measured O K-edge XAS [25,26,29,31,33,34] and hard X-ray Raman scattering [41] of liquid water at different temperatures and found that the pre-edge peak is sensitive to the temperature due to the local structural change of the HB network. The effect of temperature in liquid water has also been studied by neutron diffraction [98], nuclear magnetic resonance (NMR) [99], X-ray Compton scattering [100,101], and IR and Raman spectroscopy [102–105], and by MD simulations [105–107].

In order to solve some conflicting interpretations, we investigate the O K-edge XAS of aqueous solutions of different alkali halides systematically in reliable transmission mode [42]. Fig. 3(a) shows O K-edge XAS spectra for pure liquid water and aqueous salt solutions with different cations (3 M LiCl, 3 M NaCl, and 3 M KCl) at 25 °C. The pre-edge peak of aqueous salt solutions shows the blue shift in transition energy from that of liquid water. The energy shift of the pre-edge peak is dependent on the alkali ion, and LiCl solutions show larger blue shifts than NaCl and KCl solutions. Fig. 3(b) shows O K-edge XAS of aqueous sodium salt solutions with different anions (3 M NaCl, 3 M NaBr, and 3 M NaI). The pre-edge peak of aqueous salt solutions does not show distinct energy shifts from that of liquid water. These results suggest that the energy shift in the '$4a_1$' pre-edge peak could be caused by not the interaction of anions with water molecules but the short range interaction of cations with oxygen atoms in water molecules. On the other hand,

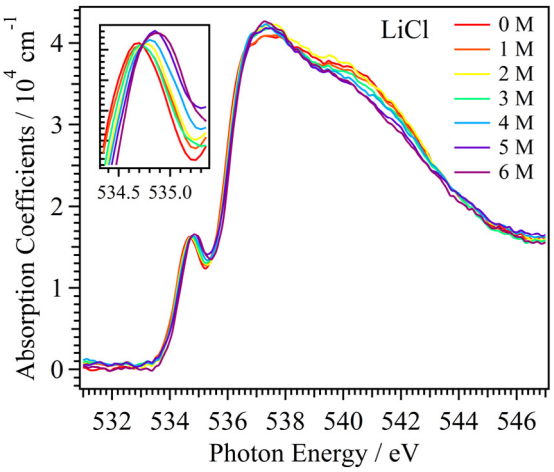

Fig. 4. O K-edge XAS spectra of LiCl solutions at different concentrations at 25 °C. The XAS spectrum of pure liquid water (0 M) is also shown. The inset shows the expansion of the pre-edge region.

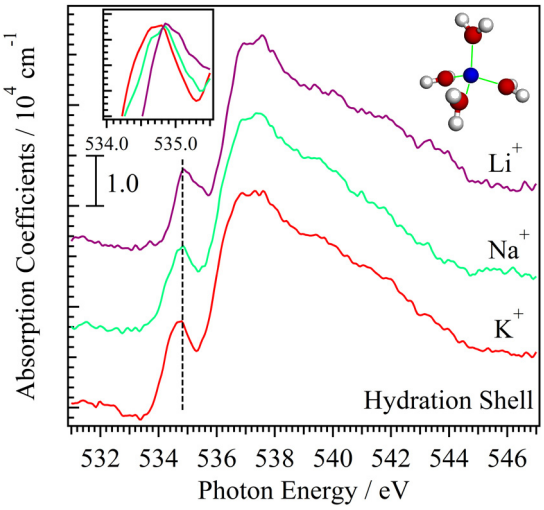

Fig. 5. O K-edge XAS spectra for the first hydration shells of the different cations (Li^+, Na^+, and K^+), which are obtained by the subtraction procedures. The dashed line in the pre-edge region is set to the peak top of the Na^+ ion. The insets show the expansion of the pre-edge region and the schematic of the hydration structures of cations.

the vibrational spectroscopy reveals the interaction of anions with water molecules from the OH stretching mode [10–12].

Fig. 4 shows the O K-edge XAS spectra of LiCl solutions at different concentrations at 25 °C. The XAS spectrum of 1 M LiCl is almost the same as that of pure liquid water (0 M). By increasing the concentration of salt solutions, the pre-edge peak is more blue-shifted. The quasi-isosbestic point is observed in the XAS spectra at different concentrations, as shown in the inset of Fig. 4. The isosbestic point in the pre-edge region suggests that the XAS spectra consist of two components: water interacted with cations and bulk liquid water. In order to observe the hydration shell of cations more clearly, we have extracted the contribution of hydrated water molecules with cations from the O K-edge XAS spectra. The coordination numbers of water molecules with cations are referred from the neutron diffraction studies [6,8], in which those of the Li^+, Na^+, and K^+ ions are 4, 5, and 6, respectively. The amount of bulk liquid water is estimated by subtracting the water molecules coordinated with cations from total amount of water molecules in aqueous salt solutions. In the 3 M LiCl solution, for example, the ratio of bulk water is calculated from the concentration of the solutions and the coordination number of Li^+ ions, and is estimated to be 78%. The O K-edge XAS spectrum of hydration shells of Li^+ ions are obtained by subtracting the XAS spectrum of bulk liquid water from that of 3 M LiCl solutions.

Fig. 5 shows the O K-edge XAS spectra of the first hydration shells of different cations (Li^+, Na^+, and K^+) obtained by subtracting the contribution of bulk water from 3 M LiCl, 3 M NaCl, and 3 M KCl solutions, respectively. Both the main edge feature around 537 eV and the post-edge feature around 540 eV are almost the same in the three salt solutions. As shown in the inset of Fig. 5, the pre-edge peaks are more blue-shifted in the order of K^+, Na^+, and Li^+ ions, in which the energy shifts of Na^+ and Li^+ ions from K^+ ions are 0.10 eV and 0.22 eV, respectively. Because the pre-edge peak reflects mainly the short range interaction of cations with water molecules, the pre-edge peak is more blue-shifted as the interaction of cations with water molecules is getting stronger in the hydration shell. These results are consistent with the previous neutron diffraction studies [6,8], in which the bond lengths of Li^+, Na^+, and K^+ ions with water molecules are 0.190 nm, 0.234 nm, and 0.265 nm, respectively.

In order to investigate the temperature effects of the hydration shell of cations, we have measured the O K-edge XAS spectra of liquid water and 5 M LiCl solutions at different temperatures, as shown in Figs. 6 and 7, respectively. As shown in the inset of Fig. 6, the pre-edge peak of pure liquid water is more red-shifted and is stronger by increasing the temperature. The HB is more weakened as the average hydrogen bond length becomes longer by increasing the temperature, resulting in both the red shift and the intensity increased in the '$4a_1$' pre-edge peak. Fig. 7 shows the O K-edge XAS spectra of 5 M LiCl solutions at different temperatures. As shown in the inset of Fig. 7, the temperature dependence is similar to that of the liquid water, but is not so large.

In order to investigate the temperature effect of only the first hydration shell of Li^+ ions, we have extracted the O K-edge XAS

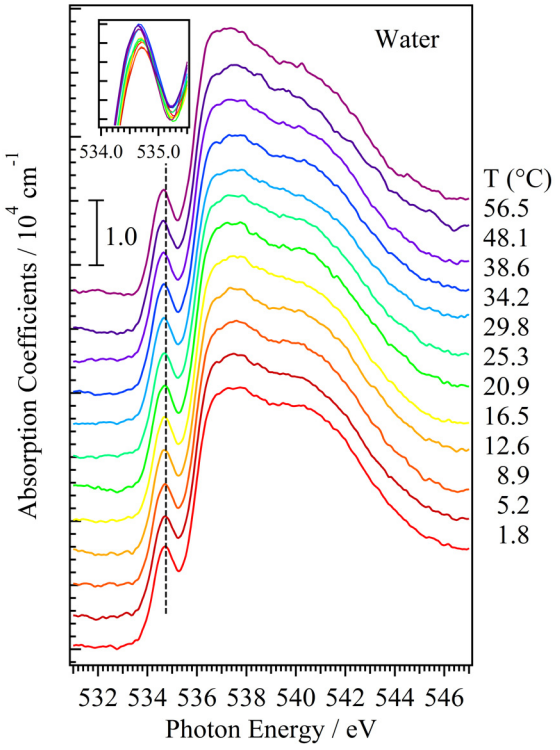

Fig. 6. O K-edge XAS spectra of liquid water at different temperatures. The dashed line in the pre-edge region is set to the spectrum at 1.8 °C. The inset shows the expansion of the pre-edge region.

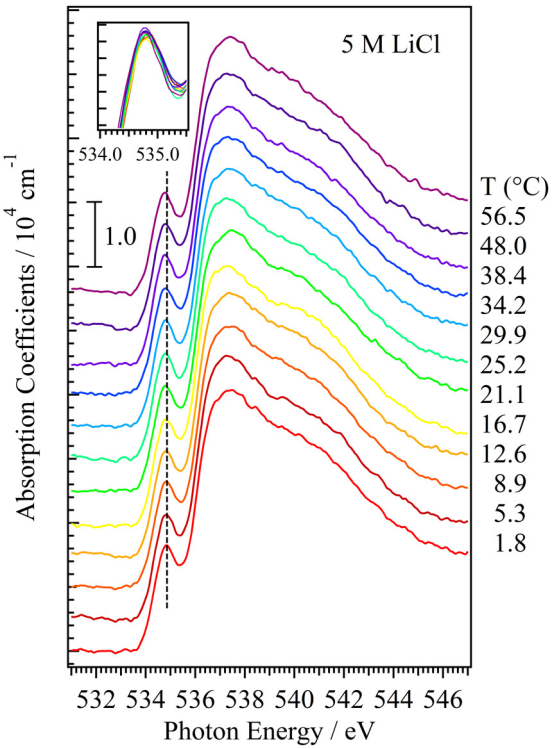

Fig. 7. O K-edge XAS spectra of 5 M LiCl solutions at different temperatures. The dashed line in the pre-edge region is set to the spectrum at 1.8 °C. The inset shows the expansion of the pre-edge region.

spectra of the first hydration shell by subtraction of liquid water spectra shown in Fig. 6 from the 5 M LiCl spectra shown in Fig. 7, assuming the oxygen coordination number fixed to 4. Fig. 8 shows the O K-edge XAS spectra of the hydration shell of the Li^+ ions at different temperatures. The spectral shapes and the energy positions of the pre-edge peaks are insensitive to the change in temperature. These results are consistent with the weak temperature dependence of the radial distribution functions (RDF) of Li^+ ions with water molecules obtained by MD simulations [81] and neutron diffraction studies [66]. The present XAS analysis has revealed that not only the RDF but also the short range interaction between Li^+ ions and water molecules are almost the same at the different

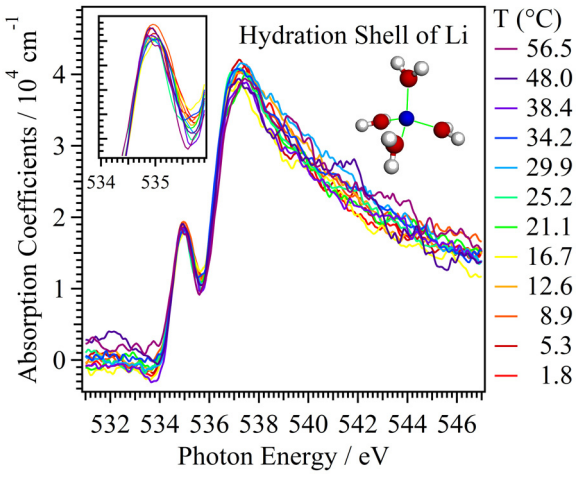

Fig. 8. O K-edge XAS spectra for the first hydration shells of Li^+ ions at different temperatures obtained by the XAS spectra of liquid water and 5 M LiCl solutions shown in Figs. 6 and 7. The inset shows the expansion of the pre-edge region.

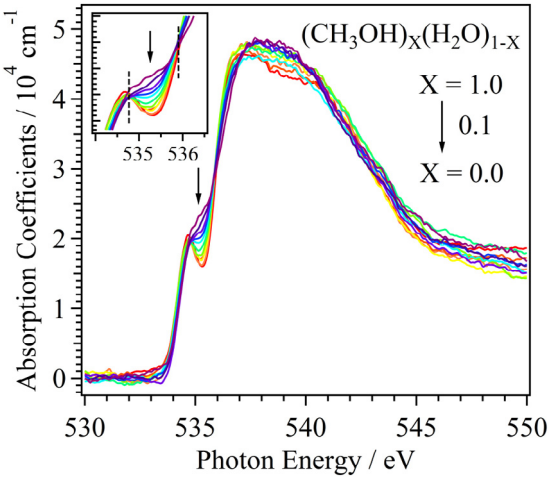

Fig. 9. O K-edge XAS spectra of aqueous methanol solutions at different concentrations at 25 °C [45]. The mixing ratio of methanol in the solution decreases with molar fraction steps of 0.1 along indicated arrows. The inset shows isosbestic points (dashed lines) in the pre-edge region.

temperatures, and has confirmed the strong hydration of the Li^+ ions in LiCl solutions.

2.3. Methanol solution

Liquid methanol shows one- and two-dimensional (1D/2D) HB networks such as chain and ring structures [108–113], and liquid water shows tetrahedrally coordinated three-dimensional (3D) HB networks [114]. The neutron diffraction studies indicated the formation of 3D HB networks of methanol–water mixtures with hydrophilic and hydrophobic interactions [7,115,116]. The interaction between methanol and water molecules in the binary solution was investigated by NMR [117], mass spectrometry [118], Rayleigh scattering [119], dielectric relaxation methods [120], and IR [121–128] and Raman spectroscopy [18,126,129–131]. These studies show nonlinear profiles at different concentrations due to the hydrophobic interactions between methanol and water molecules. The structure of liquid methanol and methanol–water binary solutions was investigated theoretically by MD [132–146] and Monte Carlo simulations [147–152]. Although the methanol–water binary solution has been extensively studied experimentally and theoretically, microscopic structures of methanol–water mixtures, such as nearest–neighbor interactions, have not yet been revealed in detail.

In this review, we investigate the local structure of methanol–water binary solutions at different concentrations by the O and C K-edge XAS [45]. Fig. 9 shows O K-edge XAS spectra for methanol–water binary solutions at different concentrations at 25 °C. The '$4a_1$' pre-edge peak of liquid water (534.7 eV) is blue-shifted and broadened by the HB interaction [26]. On the other hand, the pre-edge feature of liquid methanol (534.9 eV) is embedded in the main peak but is similarly blue-shifted from the gas-phase peak [43,44,153,154]. The intensity of the pre-edge region around 535.2 eV decreases as the molar fraction of methanol (X) decreases in the binary solution $(CH_3OH)_X(H_2O)_{1-X}$. It is known that the pre-edge peak in liquid water reflects the HB interaction, and the intensity of methanol is different from that of water. The pre-edge region shows isosbestic points at 534.8 eV and 535.9 eV. It indicates that the pre-edge region in the XAS spectrum contains only two contributions, which are the HB interaction of liquid methanol and that of liquid water. The pre-edge peak of liquid water is sensitive to the HB interaction of liquid water and is dependent on the temperature [29]. The concentration dependence in the pre-edge region of the methanol–water binary solution

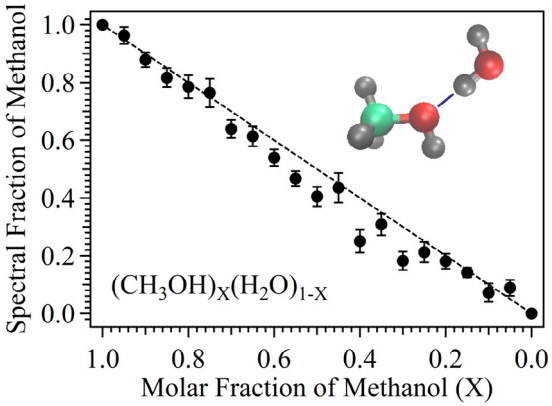

Fig. 10. Fraction of the methanol contribution in the pre-edge region of the O K-edge XAS spectra as a function of the methanol molar fraction (X) in the solutions $(CH_3OH)_X(H_2O)_{1-X}$, which is obtained by fitting from superposition of liquid methanol ($X = 1.0$) and liquid water ($X = 0.0$) [45]. Each fraction includes an error bar. The inset shows a typical HB interaction between methanol and water molecules.

is smaller than the temperature dependence of liquid water. Therefore, nearly the same HB interaction between methanol and water could be possible.

In order to obtain the change in the HB interaction at different concentrations, the pre-edge region between 534 eV and 536 eV in the O K-edge XAS spectra at different concentrations is fitted by the superposition of pure liquid methanol ($X = 1.0$) and pure liquid water ($X = 0.0$). Fig. 10 shows the fraction of the pure methanol contribution in the pre-edge region as a molar fraction step of 0.05, which corresponds to the HB interaction. The intensity decreases almost linearly as the molar fraction of methanol decreases. There may be some information about different local structures on the oxygen atom behind small deviations from the linear dependence, but it is consistent with the result of vibrational spectroscopy [126,128], which explains that the ratio of HB interaction of methanol–methanol to that of methanol–water is linearly dependent on the molar fraction of methanol.

Fig. 11 shows C K-edge XAS spectra of methanol–water binary solutions of different concentrations at 25 °C. The C K-edge XAS spectrum is more appropriate than the O K-edge XAS as regards the analysis of the intermolecular interaction of methanol because the carbon atom is contained only in methanol. The first peak around 288.4 eV arises from a transition of the C 1s electron to the lowest unoccupied orbital (8a′) of C—O antibonding and O—H bonding

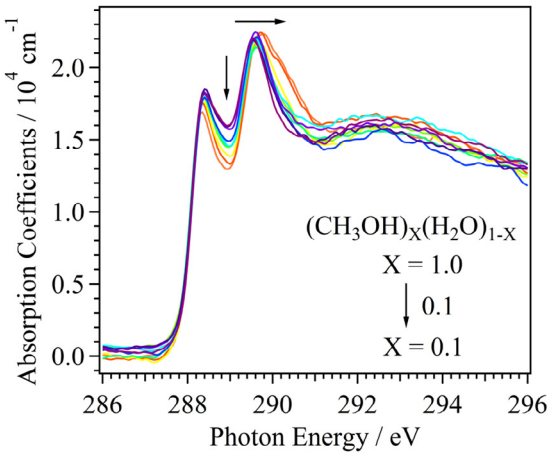

Fig. 11. C K-edge XAS spectra of aqueous methanol solutions at different concentrations at 25 °C [45]. The mixing ratio of methanol in the solution decreases with molar fraction steps of 0.1 along indicated arrows.

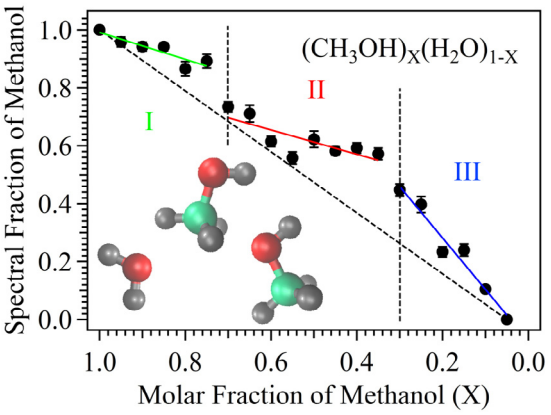

Fig. 12. Fraction of the liquid methanol contribution in the second peak in the C K-edge XAS spectra as a function of the methanol molar fraction (X) in the solutions $(CH_3OH)_X(H_2O)_{1-X}$, which is obtained by fitting from superposition of liquid methanol ($X = 1.0$) and the dilute methanol solutions ($X = 0.05$) [45]. Each fraction includes an error bar. Three characteristic regions are found with the borders of $X = 0.7$ and $X = 0.3$. The inset shows the schematics of the interactions of methyl groups in methanol molecules with methanol and water molecules.

characters, and is related to the HB interaction of OH and CH_3 groups [43,44,155,156]. This peak does not change its energy position so much at different concentrations. This is reasonable if the HB interaction of methanol with water is not so different from that with methanol and is consistent with the results of O K-edge XAS shown in Fig. 10.

On the other hand, the second peak around 289.55 eV in Fig. 11 arises from a transition of the C 1s electron to the second lowest unoccupied orbital (9a′) of pseudo CH_3-π* character with a very small OH component, and is related to the methyl group of methanol molecules. This peak increases the blue shift as the mixing ratio of water increases. It is reasonable, considering that the blue shift arises from the interaction of methyl group in methanol molecule. Liquid methanol forms 1D/2D network structures, and the methyl groups are apart from each other due to its hydrophobic interaction. When water molecules join the 1D/2D HB network of methanol, the 3D HB network might be formed. Then, the interaction of methyl groups can be enhanced in binary solutions and causes the blue shift of the second peak in the C K-edge XAS spectra. The general behavior observed is consistent with that of the neutron diffraction [7], where mixed methanol–water networks are formed and methyl groups become closer to each other in the methanol–water binary solution.

Because the second peak related to the methyl group shows a quasi-isosbestic point around 290 eV, two contributions would be contained in the second peak: One is the interaction of surrounding methanol with the methyl group, which is obtained by the C K-edge XAS spectrum of liquid methanol ($X = 1.0$). The other is the hydrophobic interaction of surrounding water with the methyl group, which is obtained by the XAS spectrum of the dilute methanol solutions ($X = 0.05$). In order to obtain the change in the hydrophobic interaction of methyl group at the different concentrations, the second peak between 288.5 eV and 290.5 eV in the C K-edge XAS spectra at the different concentrations are fitted by superposition of the reference spectra of liquid methanol ($X = 1.0$) and the dilute methanol solution ($X = 0.05$).

Fig. 12 shows the fraction of the pure liquid methanol contribution in the second peak at different molar fractions of methanol (X) in the binary solution $(CH_3OH)_X(H_2O)_{1-X}$, which corresponds to the hydrophobic interaction of the methyl group. The fraction of the pure liquid methanol contribution is changed nonlinearly and shows three different behaviors with the borders of $X = 0.7$ and $X = 0.3$. In the methanol-rich region I ($X > 0.7$), the intensity is not

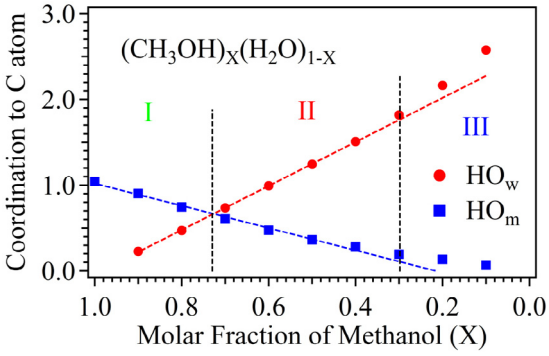

Fig. 13. Coordination numbers of HO_m and HO_w to the C atom of the methyl group in methanol molecules at different molar fractions of methanol (X) in the solutions $(CH_3OH)_X(H_2O)_{1-X}$ [45]. Below $X = 0.73$ (region II), the coordination number of HO_w becomes larger than that of HO_m. In the region III ($0.3 > X$), the linear dependence of HO_m and HO_w is not valid as shown by dashed lines.

so much changed as compared to the intensity of liquid methanol ($X = 1.0$). The phase transition-like behavior of the intensity change is found at $X = 0.7$. The slow decrease in intensity (indicating the blue shift of the second pre-edge peak) continues when increasing the mixing ratio of water in the region II ($0.7 > X > 0.3$). The decrease in intensity becomes faster in the water-rich region III ($0.30 > X > 0.05$). These results suggest different local interactions of the methyl group at the different concentration regions.

In order to reveal the concentration dependent local interactions of the methyl group, we have carried out the MD simulation by using GROMACS 4.5.5 [157]. The potential of methanol molecule is described by OPLSAA [158,159], and that of water molecule is TIP5P [160]. The temperature is controlled by the Nosé–Hoover thermostat method [161]. The pressure is adjusted by the Parrinello–Rahman method [162]. The simulation is performed at a time step of 1 fs with a periodic boundary condition and the particle-mesh Ewald method [163]. The unit cell consists of 500 molecules, and the molar fraction of methanol (X) is changed from $X = 0.0$ to $X = 1.0$. Randomly distributed structures are optimized by the simulations, which run during 50 ps at −173.15 °C in the NVT condition, 50 ps at −73.15 °C and 1 atm in the NPT condition, and 400 ps at 25 °C and 1 atm in the NPT condition. The equilibrium structures are obtained by sampling the structures every 1 ps during a simulation time of 2 ns.

First, we have calculated RDF of four different HB: O_m—HO_m, O_m—HO_w, O_w—HO_m, and O_w—HO_w. The distances of both the first peak and the first minimum point in RDF are not changed even at different molar fractions. It means that the HB interaction of water is nearly the same as that of methanol as already discussed in the O K-edge XAS. In order to obtain the coordination number of methyl group with HO_m and HO_w, we have calculated RDF of C with HO_m and HO_w at different molar fractions of methanol (X) in the solutions $(CH_3OH)_X(H_2O)_{1-X}$. Fig. 13 shows the number of the coordination by nearest neighbors HO_m and HO_w to the C atom in the methyl group of methanol at different binary solutions. The coordination is defined within the RDF distance of 3.2 Å, which is the first minimum point of HO_m and HO_w. The methyl group in liquid methanol ($X = 1.0$) is surrounded by HO_m (square). By increasing the molar fraction of water, the number of HO_m coordination decreases and instead that of HO_w (circle) increases. When the methanol molar fraction is below $X = 0.7$, the number of HO_w coordination becomes larger than the HO_m coordination. It is reasonable considering that the molar ratio of methanol and water is 2:1 at $X = 0.67$ and the ratio of the H donating site is 1:1. However, the rate of increase in the number of HO_w coordination is larger than the rate of decrease in the number of HO_m coordination. The rate of increase in the number of HO_w coordination is accelerated

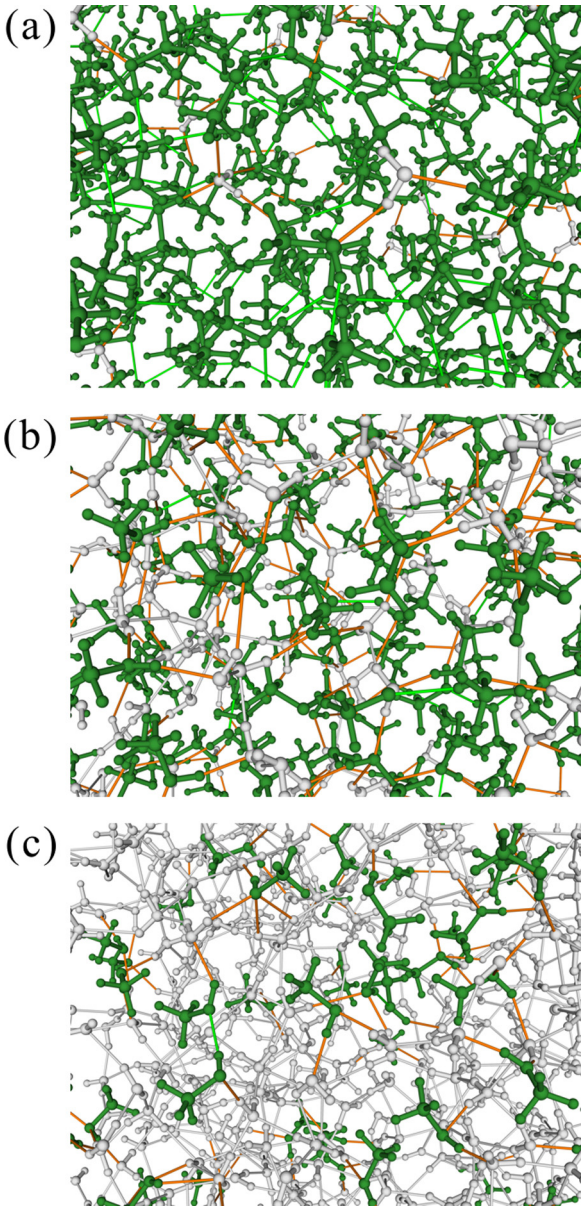

Fig. 14. Typical structures of aqueous methanol solutions at different concentrations [45]: (a) $X = 0.9$, (b) $X = 0.5$, and (c) $X = 0.1$. Methanol and water molecules are marked as green and white, respectively. HB between methanol and water is marked as an orange line.

in the region III ($0.3 > X$). On the other hand, the number of HO_m coordination is nearly zero in the region III. Note that $X = 0.7$ and $X = 0.3$ are almost the same borders in the spectral change of the C K-edge XAS.

From the result of the C K-edge XAS shown in Fig. 12, the interaction around the methyl group of methanol molecule shows characteristic changes at the three concentration regions. The MD simulations show similar three concentration regions from the coordination number around the methyl group shown in Fig. 13. Fig. 14(a) shows a typical structure in the binary solution at $X = 0.9$ in the methanol-rich region I. The average size of water-only clusters is much smaller than the total number of water molecules. Water molecules form the HB network with methanol clusters and stabilize the total energy of the binary solution. However, the interaction around the methyl group of methanol is not so much influenced by water molecules because of a small amount of isolated water molecules. It is consistent with the previous work [18,120], where

water molecules are coordinated to the terminal of methanol chains in the methanol-rich region.

Fig. 12 shows a phase-transition-like intensity change at $X = 0.7$ in the C K-edge XAS. Fig. 13 shows that the number of HO_w coordination to the methyl group becomes larger than that of HO_m coordination below $X = 0.7$. Fig. 14(b) shows a typical structure in the binary solution at $X = 0.5$ in the region II. Water molecules form a large cluster and have the 3D HB network with methanol molecules, resulting in the increase of the interaction of the methyl group in methanol with water molecules. The phase-transition-like behavior at $X = 0.7$ in the C K-edge XAS indicates that the 3D HB network involving water clusters is dominant over the 1D/2D HB network of methanol in the binary solutions. This result is consistent with the previous MD simulation, in which the 1D chain structure of methanol molecules is changed to 3D mixed clusters by adding water molecules [143].

Fig. 14(c) shows a typical structure in the binary solution at $X = 0.1$ in the water-rich region III. The HB networks between methanol molecules are mostly diminished, and methanol molecules are isolated in the 3D HB network of water. The hydration structures of methanol molecules are dominated by the 3D HB network of water, and the numbers of water coordination to the methyl group increase. As a result, the hydrophobic interaction around the methyl group is enhanced in this region, increasing the blue shift in the C K-edge XAS. The previous theoretical studies suggested that hydration structures of methanol molecules are formed in this concentration region [144,146,148], consistent with the present result.

It is known that the thermodynamic parameter such as entropy and viscosity shows an extreme value at the molar fraction of $X = 0.30$ [4,5]. Dougan et al. studied neutron diffraction experiments and MD simulations and suggested that both methanol and water molecules are percolated in this region, and the thermodynamic parameters show extreme values at the molar fraction of $X = 0.27$ [116]. It means that the structure and abundance of large mixed methanol–water HB networks in the binary solution affect macroscopic thermodynamic properties.

2.4. Pyridine solution

Pyridine is soluble in water at any concentration. In aqueous pyridine solution, the formation of HB between the N site of pyridine and the H site of water is proposed by the vibrational spectroscopy: IR [13] and Raman [14,15]. The formation of HB networks is supported by DFT [14,164,165] and Monte Carlo simulations [166]. But the local structure of aqueous pyridine solution is still unknown. The O K-edge XAS spectra of water molecules in aqueous 3-methylpyridine [167] and pyridine [168] solutions have been recently reported at different concentrations but the C and N K-edge XAS spectra of pyridine molecules have not yet been reported. In this review, we report the C and N K-edge XAS of aqueous pyridine solutions at different concentrations to investigate the molecular interaction of the C and N sites of solute pyridine with water in the binary solutions [58].

Fig. 15(a) shows the C K-edge XAS spectra of aqueous pyridine solution $(C_5H_5N)_X(H_2O)_{1-X}$ at different concentrations. The transition C 1s → π* shows two peaks: the first peak (C1) is derived from the meta and para carbon sites of pyridine. The second peak (C2) is the ortho carbon sites. By increasing the molar fraction of water in aqueous pyridine solution, the C1 peaks related to the meta and para carbon sites are red-shifted. The C2 peaks related to the ortho carbon sites are slightly blue-shifted as increasing the molar fraction of water. Fig. 15(b) shows the N K-edge XAS spectra of aqueous pyridine solutions at different concentrations. The N 1s → π* peaks are more evidently blue-shifted. These energy shifts are reasonable,

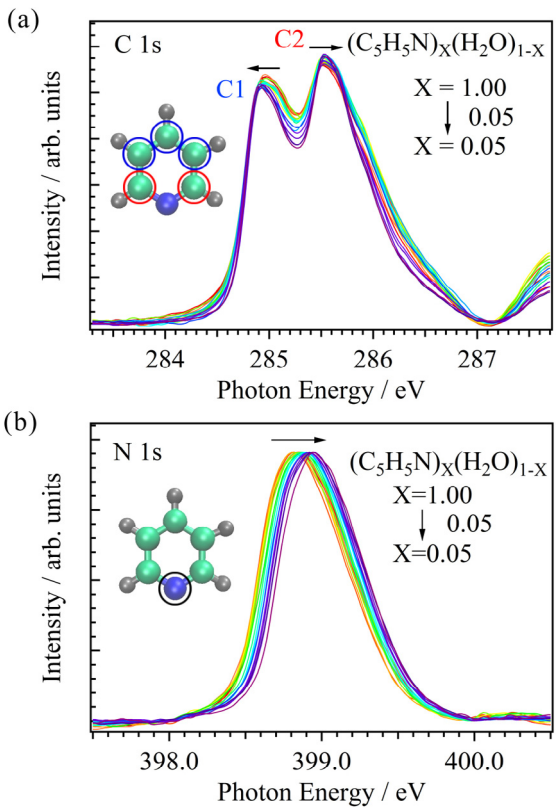

Fig. 15. XAS spectra of aqueous pyridine solutions at different concentrations in (a) C and (b) N K-edges. The peaks are shifted to the direction of arrows by increasing the molar fraction of water. The insets show the core excited atoms in pyridine molecules.

assuming that the energy shift arises from HB between the N site of pyridine and water in the aqueous pyridine solutions.

Fig. 16 shows the energy shifts of the C1, C2, and N sites of pyridine molecules at different molar fractions from liquid pyridine ($X = 1.0$). The red shift of the C1 peak is derived from the polarization effects on the core excited states in the meta and para carbon sites of pyridine molecules with surrounding water molecules with no direct HB interaction [169,170]. The blue shift of the C2 peak is explained by the balance between the red shift caused by the polarization effects on the core holes in the ortho carbon sites of pyridine with water and the blue shift caused by the short-range exchange interaction between the unoccupied π* orbital of ortho carbon atoms with nearest neighbor water molecules. The blue shift

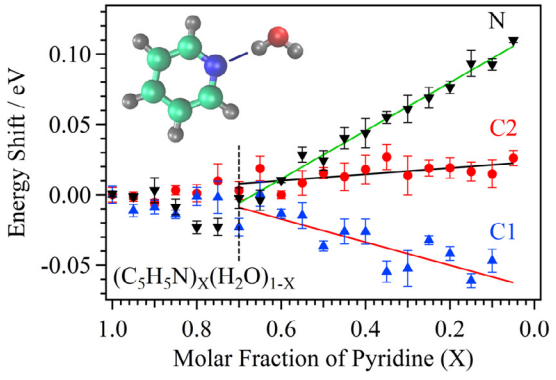

Fig. 16. The energy shifts of the C1 and C2 peaks in C K-edge XAS and the N peak in N K-edge XAS of the solutions $(C_5H_5N)_X(H_2O)_{1-X}$ from those of liquid pyridine ($X = 1.0$). The inset shows the schematics of the pyridine–water pairs in the solutions.

of the N peak is larger than that of the C2 peak. It is reasonable, considering that the direct HB interaction occurs on the N site of pyridine and that the short range exchange interaction between the π^* orbital of N sites with nearest neighbor water molecules is more important than the long-range polarization interaction.

The energy shifts of the C1, C2, and N peaks show two concentration regions with the borders of $X = 0.70$. In the region $X > 0.70$, the peaks show no energy shifts at different concentrations. Liquid pyridine shows antiparallel structures between pyridine rings by dipole interactions of pyridine molecules [171]. Because the amount of water is small in this concentration region, the antiparallel structures of pyridine dimers are preserved, and the energy position of the π^* peaks is not changed. In the region $0.70 > X$, the photon energies of the C1, C2, and N peaks are changed linearly by increasing the molar fraction of water. The number of the HB structure between the N sites of pyridine and water is increased linearly because the HB interaction is stronger than the dipole interaction between pyridine molecules. The HB structure between pyridine and water will be discussed elsewhere with the help of theoretical calculations.

2.5. Acetonitrile solution

Acetonitrile is soluble in water at any molar fraction as well as methanol and pyridine. In aqueous acetonitrile solution, two models of the acetonitrile–water dimer were proposed: one is the HB structure between the N site of acetonitrile and the H site of water, and the other is the dipole-bonded structure in which water is parallel to the C≡N group of acetonitrile by the dipole interaction. FT-IR studies of aqueous acetonitrile solutions support the formation of the HB structure from the C≡N and OH stretching modes [9,16,17] but X-ray diffraction studies support the dipole-bonded structures [9]. These two structure models are compared in MD simulations [172–175]. Recently, some groups [176,177] have reported O K-edge XAS of aqueous acetonitrile solutions and proposed that the dipole-bonded dimer is abundant in comparison with the HB structure. In this review, we report the C and N K-edge XAS of aqueous acetonitrile solutions at different concentrations, and investigate the interaction of the C≡N group in acetonitrile with water [59].

Fig. 17(a) shows the C K-edge XAS spectra of aqueous acetonitrile solutions $(CH_3CN)_X(H_2O)_{1-X}$ at different concentrations. By increasing the molar fraction of water, the peak related to the transition from C 1s to C≡N π^* unoccupied orbital is blue-shifted. Fig. 17(b) shows the N K-edge XAS spectra of aqueous acetonitrile solutions at different concentrations. The N 1s → C≡N π^* peak is slightly blue-shifted by increasing the molar fraction of water.

Fig. 18(a) and (b) shows the energy shifts of the C 1s → C≡N π^* peak and the N 1s → C≡N π^* peak, respectively, at different molar fractions of water in liquid acetonitrile. As discussed in Section 2.4, aqueous pyridine solutions form the HB between the N site of pyridine with water, and the N peak shows blue shift by increasing the molar fraction of water. On the other hand, in aqueous acetonitrile solutions, the N peak shows relatively small blue shifts. It means the ratio of the HB structure on the N site is relatively small, and the dipole-bonded structure could be dominant in aqueous acetonitrile solutions.

As shown in Fig. 18(a), the energy shift of the C peak shows three concentration regions with the borders of $X = 0.75$ and $X = 0.2$. In the acetonitrile-rich region $X > 0.75$, the C peak shows no photon energy shift. Liquid acetonitrile ($X = 1.0$) forms antiparallel structures between C≡N groups of acetonitrile by the dipole interactions [9,178]. Because the amount of water is small in this region, the antiparallel structures of acetonitrile dimers are preserved. In the region $0.75 > X > 0.2$, the mixed acetonitrile-water clusters are formed by the dipole interactions between acetonitrile and water. Because the dipole interaction between acetonitrile and water is

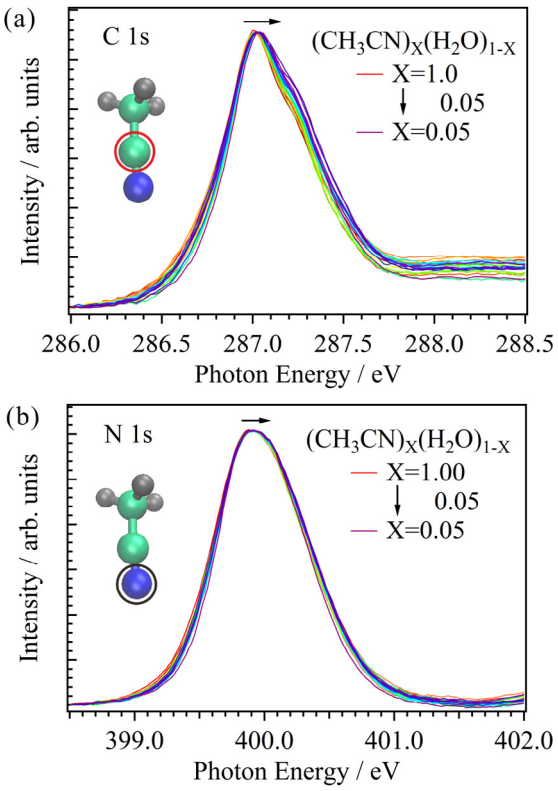

Fig. 17. XAS spectra of aqueous acetonitrile solutions at different concentrations in (a) C and (b) N K-edges. The peaks are shifted to the direction of arrows by increasing the molar fraction of water. The insets show the core excited atoms in acetonitrile molecules.

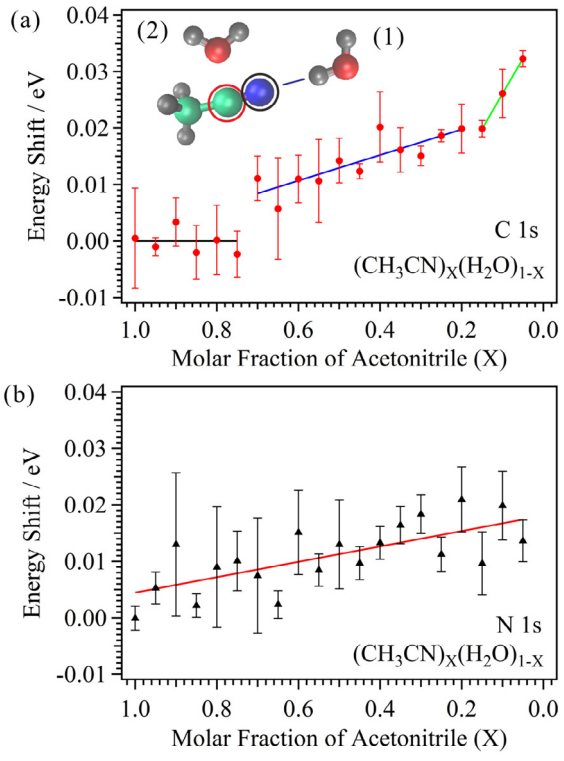

Fig. 18. The energy shifts of the peaks in XAS of the aqueous acetonitrile solutions $(CH_3CN)_X(H_2O)_{1-X}$ from those of liquid acetonitrile ($X = 1.0$) in (a) C and (b) N K-edges. The inset shows two models of the acetonitrile–water pairs in the solutions: (1) HB structures and (2) dipole-bonded structures.

weaker than the HB interaction between water molecules, acetonitrile and water are not fully mixed in this region. As a result, the energy shift of the C peak is small in this region. On the other hand, in the water-rich region $0.2 > X$, the C peak shows the larger blue shift by increasing the water ratio. Because the amount of water is large in this region, the HB between water molecules is dominant, and acetonitrile molecules are isolated in the HB network of water. The dipole interaction of acetonitrile molecules with water is increased because acetonitrile molecules are surrounded by water molecules in this region.

The microheterogeneity of aqueous acetonitrile solutions in the middle concentration region ($0.75 > X > 0.2$) has been discussed by several groups. Moreau and Douhéret have shown three concentration regions in the solutions from thermodynamic parameters such as dielectric property [179]. The microheterogeneity in the middle concentration region has been observed by small-angle neutron scattering [180] and small-angle X-ray scattering studies [181]. Mass spectrometry study shows the formation of mixed acetonitrile–water clusters in this region [182]. The present C K-edge XAS results show the three concentration regions and the microheterogeneity in the middle concentration region. The further interpretation of the microheterogeneity will be discussed elsewhere with the help of theoretical calculations.

2.6. Hydration of cyanopyrazine

Investigation of the catalytic reaction mechanism is important to obtain some clue to improvements of catalyst activity, selectivity, durability and so on. *In operando* spectroscopic observation under the reaction condition is one of the most effective ways to elucidate the mechanism. However, *in operando* spectroscopy for solid–liquid heterogeneous catalytic reactions (liquid phase reaction on solid catalyst) is difficult to measure due to interface phenomena between two condensed phases, which hinder the objective spectral change through the absorption of the probe light [183,184].

XAS in the hard X-ray region has been typically used for investigating the local structures around heavier elements (metal elements) of the catalysis in the solutions [185–188]. But it is difficult to study the conversion process from the substrate to the product because the substrate mainly consists of light elements (C, N, O, *etc.*). In order to study the conversion process in the solid–liquid heterogeneous catalytic reaction, NMR [189–191] and IR spectroscopy [192–196] have been frequently used. However, these methods have different drawback for the detection of minor components of liquid substrates. The NMR measurement requires low natural abundance isotope atoms in most of light elements, and the sensitivity is inevitably low for minor components [197]. In the IR spectroscopy, the objective peaks of minor components are often hindered by other major components. These drawbacks have often limited *in operando* measurement of solid–liquid heterogeneous catalytic reactions to the observation of main liquid substrate except for the liquid components having different absorption positions. Thus, new methodologies are still required for the *in operando* observation of the liquid substrate conversion on the solid catalyst.

XAS in the soft X-ray region has been applied to the observation of catalytic reactions such as C K-edge XAS observations of benzene oxidation on Pt(1 1 1) surface [198], water gas shift reaction on CeO_x/Au(1 1 1) [199], and $L_{II,III}$ edges of Co and Mn XAS observation of reduction behavior for Co/Mn/TiO_2 catalysts under Fischer–Tropsch synthesis [200]. However, those targets are only either gas phase substrates or solid catalysts, and the conversion of liquid substrates on the solid catalyst has not yet been investigated due to several difficulties.

In this review, we report soft X-ray XAS in transmission mode applied to *in operando* observation of solid–liquid heterogeneous catalytic reactions by using the liquid flow cell [60]. We have selected cyanopyrazine (PzCN) hydration to produce pyrazinamide ($PzCONH_2$) on the TiO_2 particle catalyst as a probe reaction shown in Eq. (1), and have investigated the reaction kinetics by the C and N K-edge XAS of liquid PzCN under the catalytic reaction.

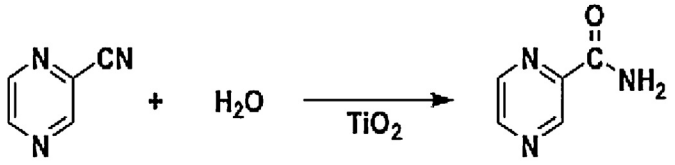

(1)

Suspension of the catalytic hydration reaction is prepared by 3.0 mL of PzCN (0.78 M), 35 mL of H_2O (45 M), 5.0 mL of ethanol (EtOH) (2.0 M) and 0.15 g of TiO_2 catalyst (3.5 mg/mL). After the liquid cell filled with 2.0 M aqueous EtOH containing 3.5 mg/mL of TiO_2 in advance is heated to the reaction temperature, the 20 mL of suspension is flowed into the liquid cell at 5.0 mL/min by using the tubing pump. Then, the measurement of the C K-edge XAS is started simultaneously with the stop of the flowing.

Fig. 19 shows C K-edge XAS spectra of PzCN hydration reaction on the TiO_2 catalyst at four different temperatures from 50.2 °C to 65.5 °C. In the spectrum of PzCN suspension, three absorption peaks (285.4 eV, 286.0 eV, and 286.6 eV) are observed. The two peaks at the lower photon energies (285.4 eV and 286.0 eV) are assigned to the excitation of carbons in the pyrazine ring from 1s to two π^* orbitals at different energy levels according to previous XAS studies of pyrazine [201,202]. The highest energy peak (286.6 eV) corresponds to the excitation of carbon in the cyano group from 1s to C≡N π^* orbital [203]. On the other hand, in the spectrum of $PzCONH_2$ suspension, one broad asymmetric shaped absorption peak (285.3 eV) is only observed in the energy region of carbon in the pyrazine ring.

All the XAS spectra shown in Fig. 19 vary the ratio of the absorption peak intensities with the reaction time. Furthermore, the variation rate increases with increasing the reaction temperature. These results clearly indicate that the catalytic reaction of PzCN can be successfully detected as the spectral change. It is notable that XAS can clearly detect the absorption peaks of PzCN and $PzCONH_2$ although these components are minor in the prepared suspensions.

In order to determine the fraction of PzCN and $PzCONH_2$ in the hydration reaction, the C K-edge XAS spectra shown in Fig. 19 were fitted by the superposition of the reference spectra of PzCN and $PzCONH_2$ in the energy region from 284 eV to 286.4 eV. To determine whether the obtained fractions of PzCN and $PzCONH_2$ are reasonable or not, we have carried out the kinetic analysis of the PzCN hydration reaction on the TiO_2 catalyst. Fig. 20 shows the logarithmic plots of the normalized fractions of PzCN for reaction time. In these plots, the PzCN fractions from the first energy scans at each temperature are approximately regarded as the data at 14 min and the next energy scans are plotted every 14 min for the C K-edge XAS. All of the plots at each temperature clearly exhibit linear relationship.

Considering the reaction mechanism of nitrile hydration on metal oxides reported in previous studies [204–208], the reaction rate is able to describe as a first order rate equation. The relationship between the concentration of PzCN and reaction time is described in the following equation:

$$\ln\frac{[\mathrm{PzCN}]}{[\mathrm{PzCN}]_0} = \frac{k_3 K_1 K_2 C_w}{(1 + K_2 C_w)^2} t \tag{2}$$

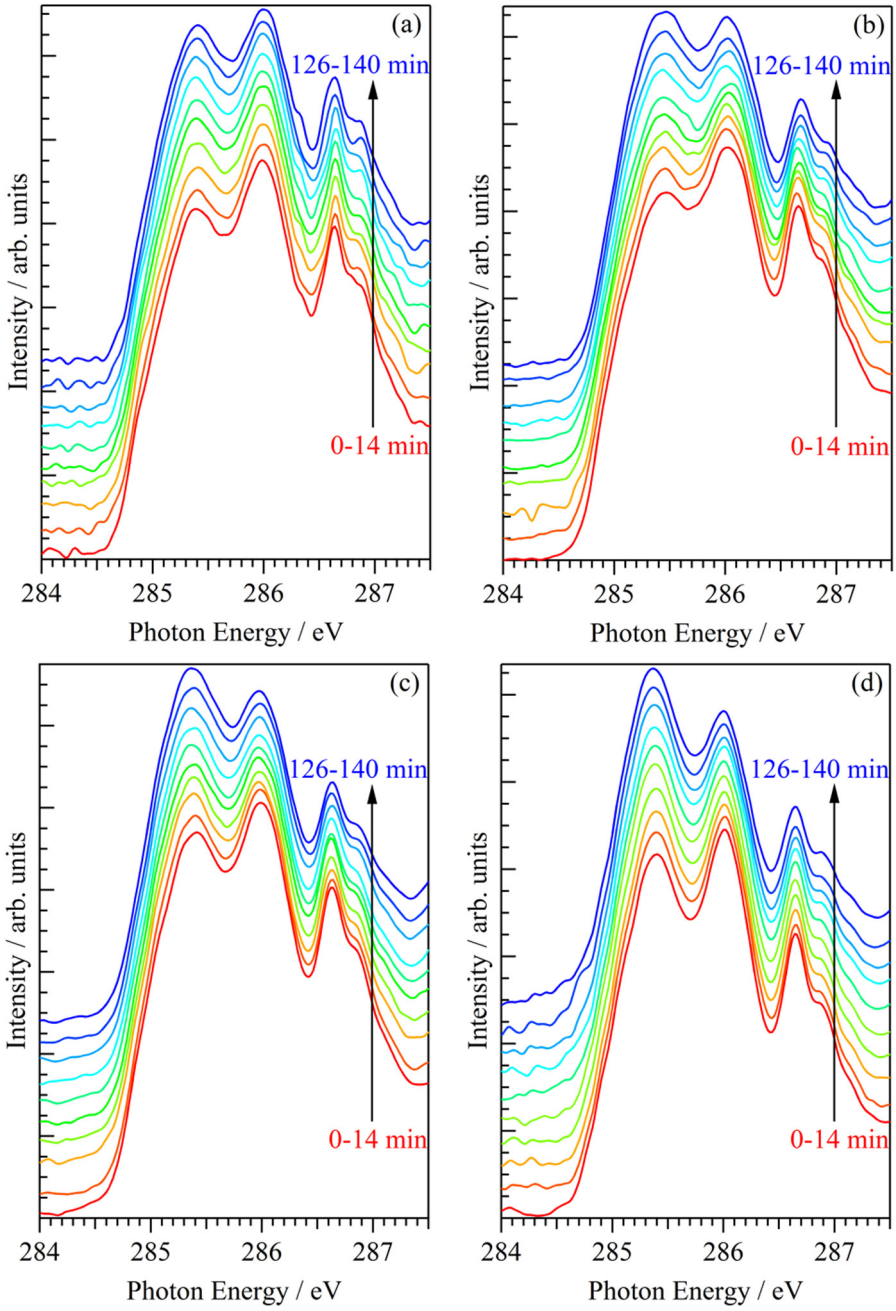

Fig. 19. C K-edge XAS spectra as a function of time during PzCN hydration reaction on the TiO_2 catalyst at (a) 50.2 °C, (b) 55.8 °C, (c) 62 °C, and (d) 65.5 °C [60]. Each spectrum was obtained by the energy scan of soft X-rays from 283 eV to 289 eV for 14 min.

where K_1, K_2, k_3, and C_w correspond to the equilibrium constant for the adsorption of PzCN, that for the adsorption of H_2O on TiO_2 surface, the rate constant for the reaction between PzCN and H_2O adsorbed on TiO_2 surface, and the constant concentration of H_2O, respectively. Thus, the gradient of the logarithmic plots in Fig. 20 are the apparent rate constants corresponding to $k_3K_1K_2C_w/(1+K_2C_w)^2$ at each temperature. We have measured N K-edge XAS spectra in the PzCN hydration reaction at three different temperatures from 52.1 °C to 71.5 °C, and obtained the fractions of PzCN and $PzCONH_2$ during the reaction.

Fig. 21 shows Arrhenius plot for the PzCN hydration reaction based on the gradient of logarithmic plots. Both the plots obtained from the C and N K-edge XAS show linear relationship. Furthermore, apparent activation energies calculated from the C and N K-edge XAS were 77 kJ/mol and 80 kJ/mol, which are comparable with those of the benzonitrile hydration reaction on $Ru(OH)_x/Al_2O_3$ catalyst (71.5 kJ/mol) [205] and the cyanopyridine hydration reaction on CeO_2 catalyst (81.7 kJ/mol for 2-cyanopyridine and 80.7 kJ/mol for 4-cyanopyridine) [207]. Therefore, the obtained rate constants from the C and N K-edge XAS could be reasonable.

3. Electrochemical reactions

To get a better understanding of electrochemistry, it is necessary to know structures of electrolytes including electric double layers at different potentials. The structures of solvent water molecules at different potentials have been studied by FT-IR [209,210], sum frequency generation [211], surface-enhanced Raman [212], and surface-enhanced IR spectroscopies [213]. The orientation of water

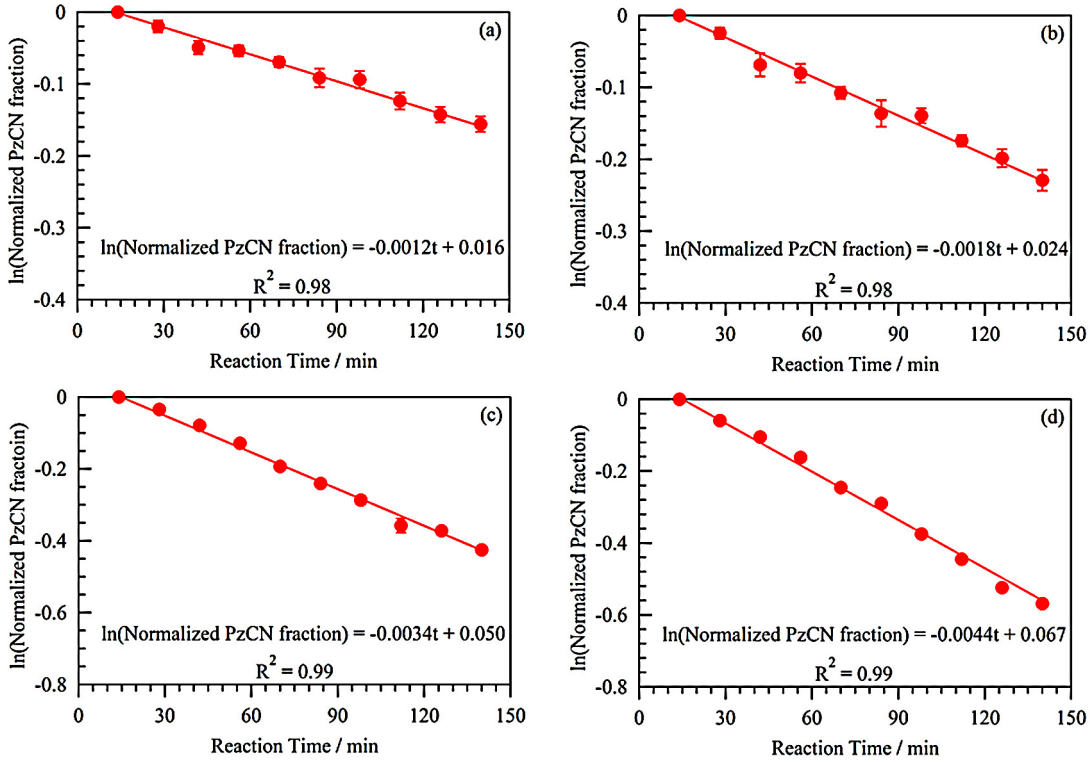

Fig. 20. Logarithmic plots of the cyanopyrazine (PzCN) fraction obtained from the fitting analysis for the time-resolved C K-edge XAS spectra during the PzCN hydration reaction on the TiO_2 catalyst at (a) 50.2 °C, (b) 55.8 °C, (c) 62 °C, and (d) 65.5 °C [60].

molecules at the first layers of Ag(1 1 1) electrodes is changed at different potentials in 0.1 M NaF as investigated by the X-ray scattering [214]. The distribution of electrodeposited nanoparticles on electrode surfaces is analyzed by transmission electron microscopy [215]. The structures of electrolyte molecules at solid–liquid interfaces of electrodes have been studied extensively by several methods, but there are few studies by direct measurement of the change in valence and structure of electrolytes with element-specific spectroscopy.

XAS in the hard X-ray region is applied to electrochemical reactions in order to study the local electronic structure of electrolytes in aqueous solutions [216–220]. Hard X-ray photoelectron spectroscopy is applied to investigate potential-induced Si oxide growth in water at the Si membrane surface [221]. XAS spectra in the hard

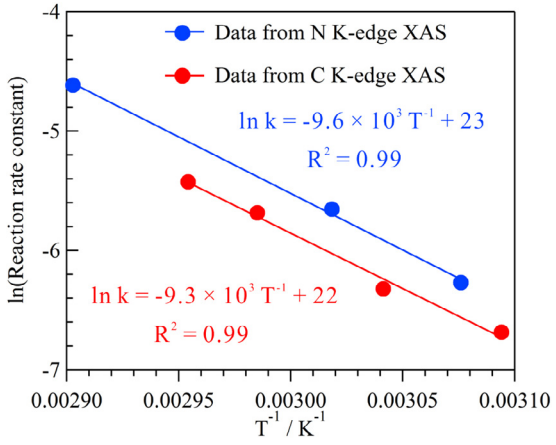

Fig. 21. Arrhenius plots for the PzCN hydration reaction on the TiO_2 catalyst based on the gradient of logarithmic plots for the PzCN fraction [60]. Red and blue circles correspond to the data from the C K-edge XAS and the N K-edge XAS, respectively.

X-ray region are easily measured in transmission or fluorescence mode due to the high transmission character of hard X-rays. On the other hand, in the soft X-ray region, several groups have developed electrochemical cells for XAS of light elements such as C, N, and O (1s), and Mn and Fe (2p) in fluorescence yields [222,223]. The *in situ* spatial measurement by scanning transmission X-ray microscope (STXM) is applied to the electrochemical reaction [224–226]. However, it is still difficult to measure *in operando* XAS of electrolytes in transmission mode during the electrochemical reaction.

3.1. Electrochemical cell

We have successfully developed an *in operando* electrochemical cell with built-in electrodes for the XAS measurement of electrolytes and electric double layers during the electrochemical reaction in the soft X-ray region. In order to study XAS of electrolytes in the electrochemical reaction, three electrodes are included in the liquid layer in region (III) of the liquid flow cell shown in Fig. 1. Fig. 22 shows schematics of the liquid cell including three electrodes [61]. The working electrode (WE) is an Au deposited on one of the Si_3N_4 membranes, which consists of Au (10 nm), Cr (5 nm), and Si_3N_4 (100 nm) multilayer films. This membrane is one side of the liquid layer and is connected with the Au tab for electrical conduction. The Teflon spacer is placed on the Si frame, opposite the Au contact. The counter electrode (CE) is a Pt mesh, which is immersed in the sample electrolyte solution. The reference electrode (RE) is Ag/AgCl immersed in a saturated KCl solution and is isolated from the liquid sample by a Teflon cover. The potential is controlled by using a potentiostat.

3.2. Electrochemical reaction of iron sulfate solution

The mechanism of the electrochemical reaction of iron sulfate solutions is investigated from the Fe L-edge XAS measurements by

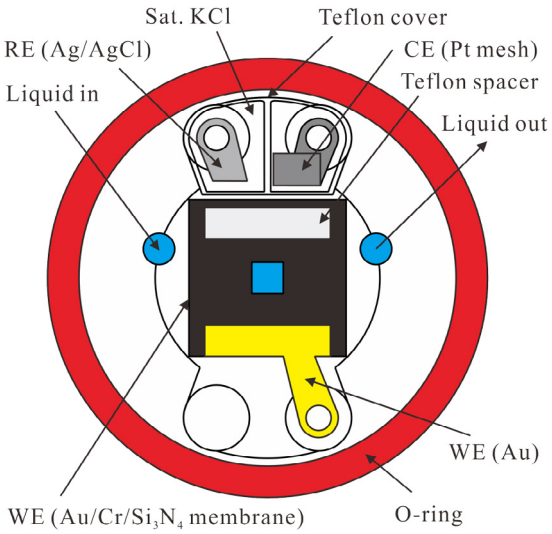

Fig. 22. Schematics of three electrodes included in the liquid layer region (III) shown in Fig. 1 [61]. The working electrode (WE) is Au-deposited on a Si_3N_4 membrane. The counter electrode (CE) is a Pt mesh. The reference electrode (RE) is Ag/AgCl immersed in a saturated KCl solution and isolated from liquid sample by a Teflon cover.

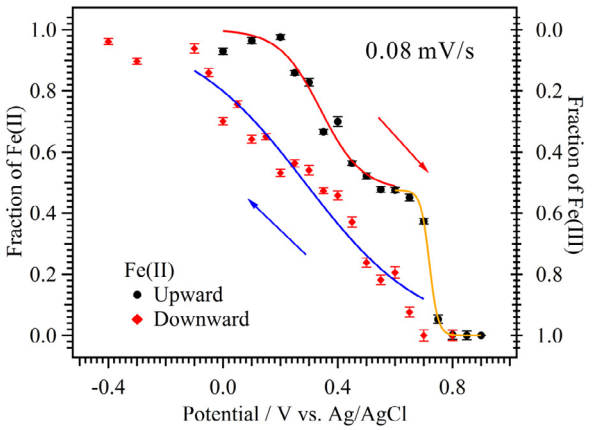

Fig. 24. Fraction of Fe(II) ions as a function of potential *versus* Ag/AgCl with saturated KCl solutions [61]. The arrows indicate the scanning direction of applied potential. The scanning rate of the potential is roughly estimated to 0.08 mV/s. Each fraction includes an error bar, which is within ±0.02. The oxidation of Fe(II) with increasing potential has two processes, whereas the reduction of Fe(III) with decreasing potential is a single process.

using the electrochemical cell [61]. Fig. 23 shows Fe L-edge XAS spectra of aqueous iron sulfate solutions at different potentials. The sample electrolyte is 0.5 M aqueous iron sulfate at pH = 2.2. The photon energy resolution at the Fe L-edge is set to 0.7 eV at BL3U in UVSOR-III Synchrotron. Each Fe L-edge XAS spectrum is measured at a constant potential and the potential is changed to the next one after finishing each XAS measurement. As shown in Fig. 23(a), the Fe L-edge XAS spectra are measured by increasing the potential from 0.00 V to 0.90 V. The amount of Fe(II) ions decreases to form Fe(III) ions nonlinearly when the potential is increased. As shown in Fig. 23(b), the XAS measurement continues while the potential is decreased from 0.90 V to −0.40 V. The amount of Fe (II) ions increases linearly from the reduction of Fe(III) to form Fe(II) ions. The XAS L_{III} spectra have signals from both Fe(II) and Fe(III) ions and show an isosbestic point, indicating that only two species are involved.

To obtain the fraction of Fe(II) and Fe(III) ions in electrochemical reactions, we fit the Fe L-edge XAS spectra at different potentials to a superposition of the reference spectra of Fe(II) and Fe(III) ions. Fig. 24 shows the fraction of Fe(II) ions (Fe(II) + Fe(III) = 1.0) as a function of potential and scanning direction. The uncertainty of the measured fractions is estimated to be within ±0.02. The central potentials of the Fe redox processes are obtained by the fits to sigmoid profiles. As a result, the oxidation of Fe(II) ions to Fe(III) ions has two processes which occur at potentials of 0.34 V and 0.72 V. The reduction of Fe(III) ions to Fe(II) ions occurs at a potential of 0.29 V.

The cyclic voltammetry (CV) measurement at the scanning rate of 5 mV/s and 20 mV/s is separately carried out to reveal the reaction mechanism. Because each XAS spectrum is obtained at a constant potential, the scanning rate of the potential is quite slow (0.08 mV/s) in the XAS measurement as compared with the CV results. The reduction peak of Fe(III) ions obtained by XAS is close to that obtained by the CV spectra. The reduction of Fe(III) ions is a simple process that reaches an equilibrium even at a scanning rate of 20 mV/s. The profile of the reduction is deviated slightly from the sigmoid profile. It might be influenced by the sulfate ions forming some complexes with Fe(III) ions [227]. Two processes are found in the case of oxidation of Fe(II) ions. One is a simple oxidation process of Fe(II) to Fe(III). This peak position is 0.72 V at 0.08 mV/s and is close to that observed in the CV spectra, suggesting that the simple oxidation process reaches an equilibrium. The peak position of the

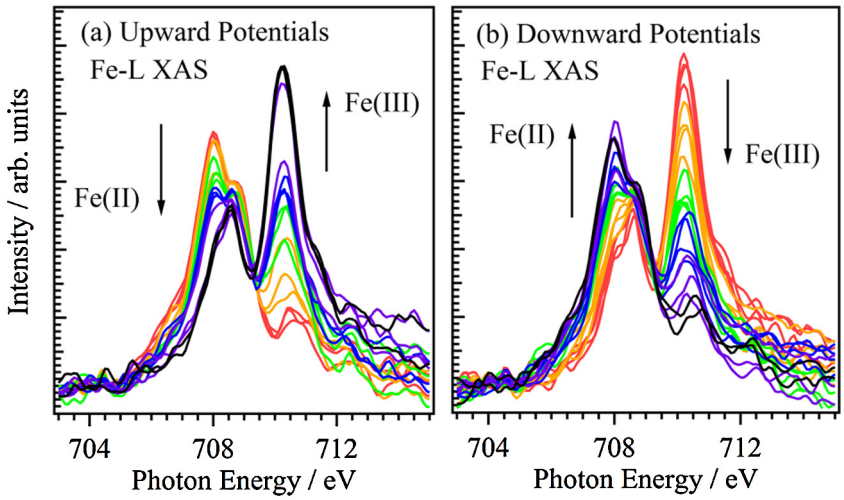

Fig. 23. Fe L-edge XAS spectra of Fe ions in a 0.5 M aqueous iron sulfate at different potentials [61]: (a) increasing from 0.00 to 0.90 V and (b) decreasing from 0.90 to −0.40 V.

other oxidation process is 0.34 V at 0.08 mV/s. In the CV spectra, the peak position is 0.57 V at 5 mV/s, and it is not observed at 20 mV/s. The reason why the peak position varies with the scanning rate is that this oxidation process does not reach an equilibrium. The rate of this process is dominantly influenced by the sulfate ions, which affect electrode kinetic parameters and diffusion coefficients [227–231]. This XAS results on the change in valence of Fe ions at different scanning rates are consistent with the CV results.

3.3. XAS with potential modulation method

In Section 3.2, each Fe L-edge XAS spectrum is measured at a constant potential and the potential is changed to the next one after finishing each XAS measurement. As a result, the scan rate of the potential corresponds to 0.08 mV/s and is quite slower than a typical scan rate of 100 mV/s in CV. CV is not applicable in such slow scan rate, and the valence of Fe ions reaches the equilibrium at each potential. Therefore, this kind of XAS measurement is not able to investigate kinetics of the electrochemical reaction. In order to investigate the kinetics of electrochemical reaction under realistic conditions, it is necessary to develop an *in operando* observation system that is able to measure XAS spectra of electrolytes at the same scan rate as in CV.

Several groups have tried spectroscopic studies of the electrochemical reaction under the same scan rate as in CV. The structures and orientations of molecules adsorbed on electrodes are investigated by IR spectroscopy at 5 mV/s [213,232]. The structural changes of electrode surfaces in electrochemical reactions are studied by *in situ* surface X-ray diffraction at several mV/s [233,234]. The surface transformation of sulfate anions on Pt(1 1 1) surfaces during the electrochemical reaction of sulfuric acid solutions is investigated by sum-frequency generation at 5 mV/s [235]. However, it is still slower than a typical scan rate of 100 mV/s in CV. There are few spectroscopic studies to observe the electrochemical reaction at 100 mV/s and to study the local structures of electrolytes and solid–liquid interfaces at electrodes in the electrochemical reaction by element-specific spectroscopy.

We have developed an *in operando* observation system for electrochemical reactions under the same scan rate as in CV by XAS with a potential modulation method [62]. The electrode potential is swept with a scan rate of 100 mV/s at a fixed photon energy, and soft X-ray absorption coefficients at different potentials are measured at the same time. By repeating the potential modulation at each fixed photon energy, it is possible to obtain XAS spectra of the electrochemical reaction at the same scan rate as in CV.

By using the newly-developed *in operando* XAS system, we demonstrate the potential-modulated Fe L-edge XAS measurement of aqueous iron sulfate solutions in electrochemical reactions at 50 mV/s and 100 mV/s. The sample electrolyte is 0.5 M aqueous iron sulfate at pH = 2.2. The temperature of the electrolyte is 27 °C. The photon energy resolution is set to 0.7 eV at BL3U in UVSOR-III Synchrotron. Fig. 25 shows the change of the potential and the soft X-ray transmission signals. The scan rate of the potential is 100 mV/s, the same as in CV. Fig. 25(a) shows the electrode potential *versus* Ag/AgCl with saturated KCl solutions. The potential is increased from 0.0 V to 1.0 V after receiving the trigger signal, then decreased to −0.4 V, and increased to 0.0 V again. The one cycle of the potential modulation takes 28 s. Fig. 25(b) shows the changes of the soft X-ray transmission during the potential modulation at the different photon energy measured by the multichannel scaler. The dwell time is set to 0.5 s, which corresponds to the potential step of 0.05 V. The soft X-ray transmission at 705 eV is not changed at different potentials because it is the region below the Fe L-edge. The absorption of Fe(II) ions is maximum at the photon energy of 708 eV. The transmission is increased when the potential is increased, and shows a maximum value at 10 s, which

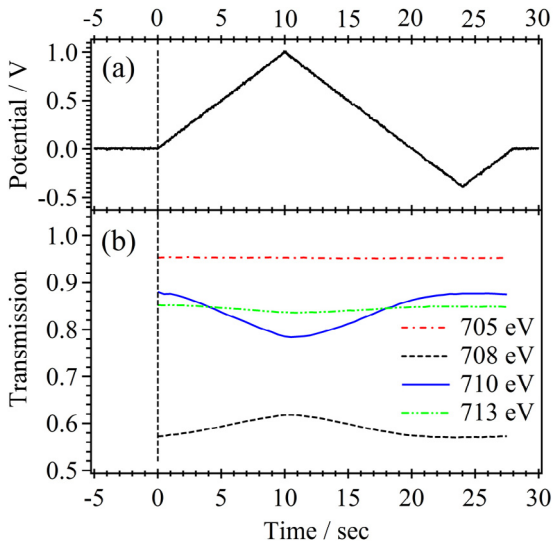

Fig. 25. Changes in soft X-ray transmission observed by modulating the potential of the electrodes at a fixed photon energy [62]. One cycle of the potential modulation takes 28 s at 100 mV/s. Both the potential modulations and the soft X-ray transmission measurements are started at 0 s. (a) The electrode potential and (b) the soft X-ray transmission at several photon energies as a function of time.

corresponds to the potential of 1.0 V. Then, it is decreased again in the downward potential after 10 s. On the other hand, the transmission at 710 eV is decreased in the upward potential, and is increased in the downward potential, because the absorption of Fe(III) ions is maximum at 710 eV. The photon energy of 713 eV is the region above the edge-jump. The transmission is slightly decreased in the upward potential due to the formation of Fe(III) ions.

3.4. Fe redox reaction at different scan rates

In operando XAS spectra of the electrochemical reaction of aqueous iron sulfate solutions can be obtained by summation of the reference soft X-ray transmission of Fe(II) ions and the difference spectra at different potentials from Fe(II). The change in soft X-ray transmission with the potential modulation is measured at different photon energies from 704 eV to 714 eV with a step of 0.1 eV. The difference spectra of soft X-ray transmission at different potentials are obtained from that at −0.4 V, where Fe(II) ions only exist by the reduction of Fe(III). The intensities I_0 is for pure liquid water. Fig. 26 shows 3D plots of Fe L-edge XAS spectra for the electrochemical reaction of iron sulfate solution at 100 mV/s. By increasing the potential from 0.0 V to 1.0 V, the peak intensity of Fe(II) is decreased and that of Fe(III) is increased. When the potential is decreased from 1.0 V to −0.4 V, the peak intensity of Fe(II) is increased and that of Fe(III) is instead decreased. The isosbestic point is found at 709.2 eV, and the intensities of Fe(II) and Fe(III) ions are changed continuously at different potentials. Previously, the XAS spectra at constant potentials needed long acquisition time and it is difficult to observe small spectral changes in electrochemical reactions. The potential-modulated XAS measurement enables us to investigate a subtle spectral change in the electrochemical reaction.

Fig. 27(a) shows the CV spectra of aqueous iron sulfate solution at 100 mV/s. The oxidation of Fe(II) to Fe(III) ions with increasing potential is observed as the peak at 0.76 V. The reduction of Fe(III) to Fe(II) ions with decreasing potential is observed as the peak at 0.19 V. In order to compare the CV spectra with the XAS spectra, the fraction of Fe(II) and Fe(III) ions is determined by fitting the XAS spectra to a superposition of the reference spectra of Fe(II) and Fe(III) ions. Fig. 27(b) shows change in valence of Fe ions in aqueous iron sulfate solution during the electrochemical reaction

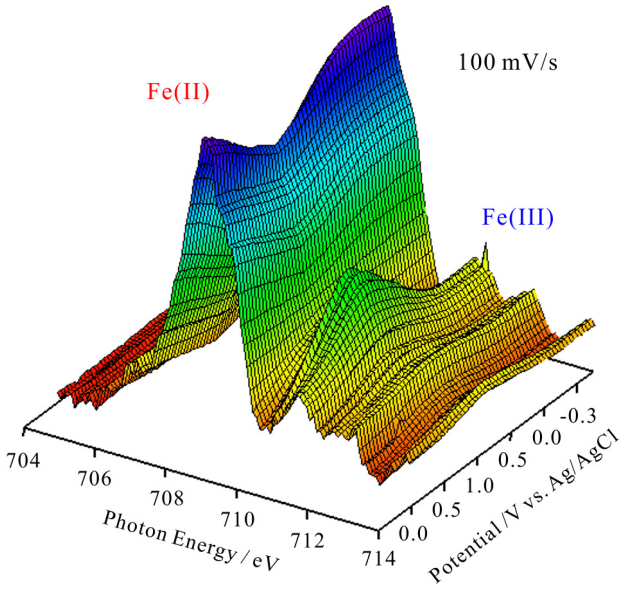

Fig. 26. 3D plots of the Fe L-edge XAS spectra in the electrochemical reaction of aqueous iron sulfate solution at 100 mV/s [62]. One axis is photon energy, and the other is the applied potential *versus* Ag/AgCl.

at 100 mV/s. The error of the fraction at 100 mV/s is within ±2%. By increasing the potential from 0.0 V to 1.0 V, the fraction of Fe(II) ions decreases and that of Fe(III) ions increases. The fraction of Fe(III) at 1.0 V is 0.26. The Fe(II) ions are partially changed to the Fe(III) ions by the oxidation process. The central potentials of the Fe redox reaction are obtained by fitting the fraction change of Fe(III) ions with sigmoid profiles. The central potential of the oxidation process by increasing the potential is 0.59 V and that of the reduction process by decreasing the potential is 0.39 V. These potentials are different from that obtained by CV at 100 mV/s; the central potential of the oxidation process obtained by XAS is lower than that obtained by CV, and the central potential of the reduction process obtained by XAS is higher than that obtained by CV.

Fig. 27(c) shows change in valence of Fe ions at 50 mV/s obtained by the potential-modulated XAS. The error of the fraction at 50 mV/s is within ±4%. The fraction of Fe(III) at 1.0 V is 0.44, and is larger than that at 100 mV/s. The central potentials of the oxidation and the reduction processes at 50 mV/s are 0.62 V and 0.43 V, respectively. These central potentials are not different from those at 100 mV/s.

The current peaks in CV reflect changes in valence of Fe ions at the solid–liquid interface of a gold electrode. On the other hand, as shown in the inset of Fig. 27, the XAS spectra include both the solid-liquid interface and the bulk electrolyte. The change in valence of Fe ions in the bulk electrolyte is influenced by the diffusion of Fe ions in the solution. When the scan rate is fast, the fraction change of Fe ions in the bulk electrolyte is slower than that at the solid–liquid interface. That is why the central potentials in the upward scan direction obtained by XAS are lower than those obtained by CV, and the central potentials in the downward potentials obtained by XAS are higher than those obtained by CV. The diffusion of Fe ions explains that the maximum fraction of Fe(III) ions at 50 mV/s is larger than that at 100 mV/s.

The current peaks in CV reflect the Fe redox reaction at the solid–liquid interface; on the other hand, the XAS spectra include both the solid–liquid interface and the bulk electrolyte. The change in valence of Fe ions in the bulk electrolyte is influenced by the diffusion of Fe ions, and the central potentials are dependent with the scan rate. The XAS spectra for different thickness of the liquid layer may distinguish the change in valence of Fe ions at the solid–liquid interface and in the bulk electrolyte.

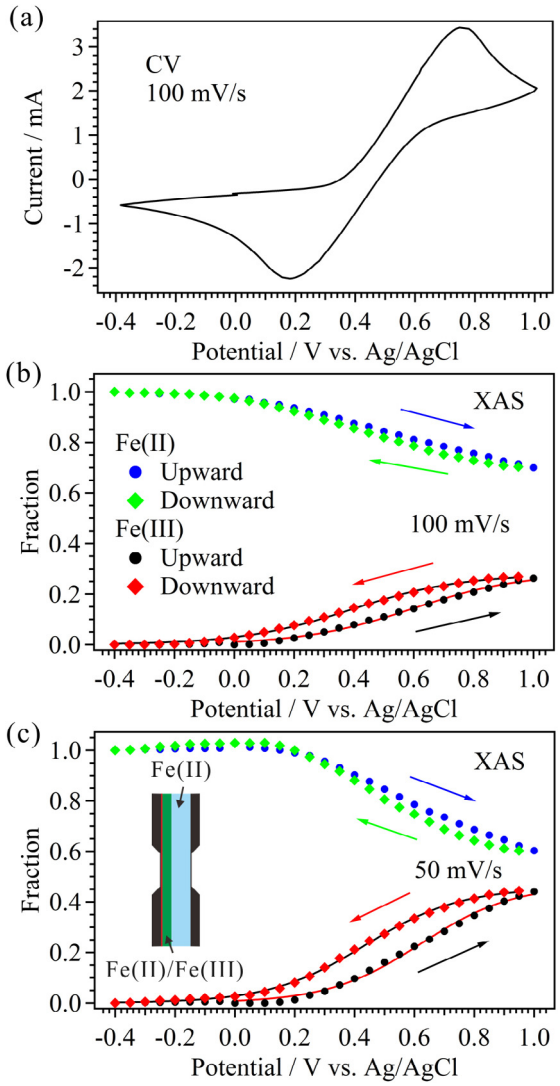

Fig. 27. (a) CV spectra of aqueous iron sulfate solution at 100 mV/s. Fractions of Fe(II) and Fe(III) ions as a function of potential *versus* Ag/AgCl in the electrochemical reaction of iron sulfate solutions at the scan rates of (b) 100 mV/s and (c) 50 mV/s [62]. The inset shows that the liquid layer consists of the solid–liquid interface of the gold electrode and the bulk electrolyte of Fe(II) ions.

4. Summary and future perspectives

We have described the development of widely-applicable liquid flow cells for the XAS measurement in transmission mode [30]. By using a simplest version of the liquid flow cells, we have investigated the local structures of aqueous alkali halide [42], methanol [45], pyridine [58], and acetonitrile solutions [59]. In aqueous salt solutions, the pre-edge peaks in O K-edge XAS are sensitive to the interactions of cations with water molecules. The energy shifts of the pre-edge peaks in different cations (Li^+, Na^+, and K^+) reflect the bond lengths between cations and hydrated water molecules. Temperature dependent XAS measurements of LiCl solutions have revealed that the first hydration shell of Li^+ ions is insensitive to the change in temperature due to the strong Li^+ and water binding.

In aqueous methanol solutions, the local structures at different concentrations have been investigated by O and C K-edge XAS. The pre-edge peak in O K-edge XAS reflects the HB interaction of oxygen atoms and shows almost linear concentration dependence. It indicates that the HB interaction of methanol with surrounding water molecules is nearly the same as in pure liquid methanol and the HB interaction of water with surrounding methanol molecules is

nearly the same as in pure liquid water. On the other hand, the C K-edge XAS enables us to study local structures around the methyl group of methanol molecules in the binary solutions, and the peak assigned to the hydrophobic interaction of methyl groups shows nonlinear profile with three concentration regions. With the help of the MD simulations, we have successfully discussed the three characteristic local structures from the hydrophobic interactions of the methyl groups: methanol-dominant 1D/2D HB network structures with isolated water molecules, methanol-water mixed 3D HB network structures, and water-dominant 3D HB network structures with isolated methanol molecules.

In aqueous pyridine solutions, we have measured C and N K-edge XAS spectra of solute pyridine molecules at different concentrations. The energy shifts of the C 1s → π* and N 1s → π* peaks indicate that the HB networks are formed between the N atom of pyridine molecules with water molecules. On the other hand, in aqueous acetonitrile solutions, the blue shift of the C 1s → C≡N π* peak is larger than the shift of the N 1s → C≡N π* peak by increasing the molar fraction of water. It indicates the dipole-bonded structure of the water molecule parallel to the C≡N group of acetonitrile is more abundant than the HB structures between the N atom in acetonitrile with water molecules. The concentration dependent C K-edge XAS measurement shows the nonlinear change of the C≡N peaks with three concentration regions, which is similar to the case of aqueous methanol solutions.

We have extended this transmission XAS technique for aqueous solutions to *in situ*/*operando* observation of catalytic and electrochemical reactions. In the catalytic reaction, we have investigated solid–liquid heterogeneous PzCN hydration reaction to produce $PzCONH_2$ on the TiO_2 catalyst from the successive measurements of C and N K-edge XAS spectra by using the liquid flow cell [60]. Variation in the C and N K-edge XAS spectra corresponding to the production of $PzCONH_2$ during the reaction is clearly observed, regardless of the coexistence of bulk liquid components. *In operando* XAS observation of the catalytic reaction can reveal even the reaction kinetics at different temperatures. Compared with the widely used spectroscopies (*e.g.*, IR, NMR), the merit of this method is the separable detection of the conversion of the minor liquid component under the reaction condition. Especially, the hindrance of bulk liquid water can be perfectly removed.

In the electrochemical reaction, the change in valence of Fe ions in aqueous iron sulfate solutions is investigated by the Fe L-edge XAS at different potentials by using an electrochemical cell with built-in electrodes [61]. Each XAS spectrum is measured at a constant potential and the potential is changed to the next one after finishing each XAS measurement. The scanning rate of this type of measurement (0.08 mV/s) is quite slower than that of CV (typically 100 mV/s). Therefore, we have developed an *in operando* observation system for the electrochemical reaction under the same scan rate as in CV [62]. The electrode potential is swept with a scan rate of 100 mV/s at a fixed photon energy. By repeating the potential modulation at each fixed photon energy, XAS of the electrochemical reaction is realized at the same scan rate as in CV.

The present *in situ*/*operando* transmission cell for the catalytic reaction is widely applicable to distinguish between the bulk liquid reactant and the product in chemical reactions. In the future, it will be realized to detect the interaction between liquid substrate and solid catalyst and the contribution of intermediate species and solvent molecules under the reaction. The *in situ*/*operando* transmission cell for the electrochemical reaction makes it possible to measure not only the valence of ions but also the local structures of aqueous solutions, and will open a possibility to reveal the adsorption structural change of water molecules in electric double layers at different potentials. This system will be applicable to study the mechanism of photo-electrochemical reactions such as a dye sensitized solar cell. The present liquid cell is also applicable to time- and spatial-resolved XAS of liquid samples. In time-resolved measurements, the mechanism of photochemical reactions will be studied by pumping liquid samples with pico–femto second laser pulses [236,237]. It is also important to apply XAS of liquid samples to spatial-resolved measurements. Recently, soft X-ray transmission microscope (STXM) is developed to measure XAS with the spatial resolution of about 30 nm [238]. We have already developed an *in situ*/*operando* liquid flow cell for the STXM system installed at the beamline BL4U in UVSOR-III Synchrotron [239]. The phase transition mechanism of liquid will be studied by spatial-resolved XAS of the liquid–liquid interface. The electro-deposition process on the electrode surface [226] will be studied by the STXM using the electrochemical cell.

Acknowledgements

The work described in this review is supported by JSPS Grants-in-Aid for Scientific Research (JSPS KAKENHI Grant nos. 20350014, 23245007, 23685006, 26248010, and 26810010). One of the authors (Y. H.) appreciates the JSPS Research Fellowship for Young Scientist. We appreciate Mr. Toshio Horigome and Dr. Takaki Hatsui for their technical contributions to develop the liquid flow cells, Prof. Adam. P. Hitchcock for his relevant advice and contribution to study of the electrochemical reaction, and Dr. Kenji Mochizuki and Mr. Valentin Leloup for their contribution to the MD simulations. We also acknowledge various kind supports from the staff members of UVSOR-III Synchrotron.

References

[1] H. Ohtaki, T. Radnai, Chem. Rev. 93 (1993) 1157.
[2] H.D.B. Jenkins, Y. Marcus, Chem. Rev. 95 (1995) 2695.
[3] Y. Marcus, Chem. Rev. 109 (2009) 1346.
[4] H.S. Frank, M.W. Evans, J. Chem. Phys. 13 (1945) 507.
[5] S.Z. Mikhail, W.R. Kimel, J. Chem. Eng. Data 6 (1961) 533.
[6] N. Ohtomo, K. Arakawa, Bull. Chem. Soc. Jpn. 52 (1979) 2755.
[7] S. Dixit, J. Crain, W.C.K. Poon, J.L. Finney, A.K. Soper, Nature 416 (2002) 829.
[8] R. Mancinelli, A. Botti, F. Bruni, M.A. Ricci, A.K. Soper, J. Phys. Chem., B 111 (2007) 13570.
[9] T. Takamuku, M. Tabata, A. Yamaguchi, J. Nishimoto, M. Kumamoto, H. Wakita, T. Yamaguchi, J. Phys. Chem., B 102 (1998) 8880.
[10] W. Rudolph, M.H. Brooker, C.C. Pye, J. Phys. Chem. 99 (1995) 3793.
[11] R. Li, Z. Jiang, F. Chen, H. Yang, Y. Guan, J. Mol. Struct. 707 (2004) 83.
[12] J.D. Smith, R.J. Saykally, P.L. Geissler, J. Am. Chem. Soc. 129 (2007) 13847.
[13] H. Takahashi, K. Mamola, E.K. Plyler, J. Mol. Spectrosc. 21 (1966) 217.
[14] S. Schlücker, R.K. Singh, B.P. Asthana, J. Popp, W. Kiefer, J. Phys. Chem., A 105 (2001) 9983.
[15] E.R. Berg, S.A. Freeman, D.D. Green, D.J. Ulness, J. Phys. Chem., A 110 (2006) 13434.
[16] D. Jamroz, J. Stangret, J. Lindgren, J. Am. Chem. Soc. 115 (1993) 6165.
[17] J.E. Bertie, Z. Lan, J. Phys. Chem., B 101 (1997) 4111.
[18] S. Dixit, W.C.K. Poon, J. Crain, J. Phys.: Condes. Matter 12 (2000) L323.
[19] A.P. Hitchcock, A.T. Wen, E. Rühl, Chem. Phys. 147 (1990) 51.
[20] G. Cressey, C.M.B. Henderson, G. Van der Laan, Phys. Chem. Miner. 20 (1993) 111.
[21] K.M. Lange, A. Kothe, E.F. Aziz, Phys. Chem. Chem. Phys. 14 (2012) 5331.
[22] U. Bergmann, P. Glatzel, S.P. Cramer, Microchem. J. 71 (2002) 221.
[23] M. Cavalleri, H. Ogasawara, L.G.M. Pettersson, A. Nilsson, Chem. Phys. Lett. 364 (2002) 363.
[24] S. Myneni, Y. Luo, L.-Å. Näslund, M. Cavalleri, L. Ojamäe, H. Ogasawara, A. Pelmenschikov, P. Wernet, P. Väterlein, C. Heske, Z. Hussain, L.G.M. Pettersson, A. Nilsson, J. Phys.: Condens. Matter 14 (2002) L213.
[25] J.D. Smith, C.D. Cappa, K.R. Wilson, B.M. Messer, R.C. Cohen, R.J. Saykally, Science 306 (2004) 851.
[26] P. Wernet, D. Nordlund, U. Bergmann, M. Cavalleri, M. Odelius, H. Ogasawara, L.-Å. Näslund, T.K. Hirsch, L. Ojamäe, P. Glatzel, L.G.M. Pettersson, A. Nilsson, Science 304 (2004) 995.
[27] L.-Å. Näslund, J. Lüning, Y. Ufuktepe, H. Ogasawara, P. Wernet, U. Bergmann, L.G.M. Pettersson, A. Nilsson, J. Phys. Chem., B 109 (2005) 13835.
[28] M. Odelius, M. Cavalleri, A. Nilsson, L.G.M. Pettersson, Phys. Rev. B: Condens. Matter 73 (2006) 024205.
[29] C. Huang, K.T. Wikfeldt, T. Tokushima, D. Nordlund, Y. Harada, U. Bergmann, M. Niebuhr, T.M. Weiss, Y. Horikawa, M. Leetmaa, M.P. Ljungberg, O. Takahashi, A. Lenz, L. Ojamäe, A.P. Lyubartsev, S. Shin, L.G.M. Pettersson, A. Nilsson, Proc. Natl. Acad. Sci. U.S.A. 106 (2009) 15214.
[30] M. Nagasaka, T. Hatsui, T. Horigome, Y. Hamamura, N. Kosugi, J. Electron Spectrosc. Relat. Phenom. 177 (2010) 130.

[31] T. Pylkkänen, A. Sakko, M. Hakala, K. Hämäläinen, G. Monaco, S. Huotari, J. Phys. Chem., B 115 (2011) 14544.
[32] S. Schreck, G. Gavrila, C. Weniger, P. Wernet, Rev. Sci. Instrum. 82 (2011) 103101.
[33] J. Meibohm, S. Schreck, P. Wernet, Rev. Sci. Instrum. 85 (2014) 103102.
[34] J.A. Sellberg, S. Kaya, V.H. Segtnan, C. Chen, T. Tyliszczak, H. Ogasawara, D. Nordlund, L.G.M. Pettersson, A. Nilsson, J. Chem. Phys. 141 (2014) 034507.
[35] L.-Å. Näslund, D.C. Edwards, P. Wernet, U. Bergmann, H. Ogasawara, L.G.M. Pettersson, S. Myneni, A. Nilsson, J. Phys. Chem., A 109 (2005) 5995.
[36] C.D. Cappa, J.D. Smith, B.M. Messer, R.C. Cohen, R.J. Saykally, J. Phys. Chem., B 110 (2006) 1166.
[37] C.D. Cappa, J.D. Smith, B.M. Messer, R.C. Cohen, R.J. Saykally, J. Phys. Chem., B 110 (2006) 5301.
[38] C.P. Schwartz, J.S. Uejio, A.M. Duffin, W.S. Drisdell, J.D. Smith, R.J. Saykally, Chem. Phys. Lett. 493 (2010) 94.
[39] I. Waluyo, C. Huang, D. Nordlund, T.M. Weiss, L.G.M. Pettersson, A. Nilsson, J. Chem. Phys. 134 (2011) 224507.
[40] I. Juurinen, T. Pylkkänen, K.O. Ruotsalainen, C.J. Sahle, G. Monaco, K. Hämäläinen, S. Huotari, M. Hakala, J. Phys. Chem., B 117 (2013) 16506.
[41] I. Waluyo, D. Nordlund, U. Bergmann, D. Schlesinger, L.G.M. Pettersson, A. Nilsson, J. Chem. Phys. 140 (2014) 244506.
[42] M. Nagasaka, T. Hatsui, N. Kosugi, UVSOR Activity Report 2010, 2011, pp. 58.
[43] K.R. Wilson, M. Cavalleri, B.S. Rude, R.D. Schaller, T. Catalano, A. Nilsson, R.J. Saykally, L.G.M. Pettersson, J. Phys. Chem., B 109 (2005) 10194.
[44] Y. Tamenori, K. Okada, O. Takahashi, S. Arakawa, K. Tabayashi, A. Hiraya, T. Gejo, K. Honma, J. Chem. Phys. 128 (2008) 124321.
[45] M. Nagasaka, K. Mochizuki, V. Leloup, N. Kosugi, J. Phys. Chem., B 118 (2014) 4388.
[46] B.X. Yang, J. Kirz, Phys. Rev. B: Condens. Matter 36 (1987) 1361.
[47] M.D. Gotz, M.A. Soldatov, K.M. Lange, N. Engel, R. Golnak, R. Könnecke, K. Atak, W. Eberhardt, E.F. Aziz, J. Phys. Chem. Lett. 3 (2012) 1619.
[48] T.Z. Regier, A.J. Achkar, D. Peak, J.S. Tse, D.G. Hawthorn, Nat. Chem. 4 (2012) 765.
[49] M.A. Soldatov, K.M. Lange, M.D. Gotz, N. Engel, R. Golnak, A. Kothe, E.F. Aziz, Chem. Phys. Lett. 546 (2012) 164.
[50] B. Hetényi, F. De Angelis, P. Giannozzi, R. Car, J. Chem. Phys. 120 (2004) 8632.
[51] M. Leetmaa, M. Ljungberg, H. Ogasawara, M. Odelius, L.-Å. Näslund, A. Nilsson, L.G.M. Pettersson, J. Chem. Phys. 125 (2006) 244510.
[52] D. Prendergast, G. Galli, Phys. Rev. Lett. 96 (2006) 215502.
[53] J.D. Smith, C.D. Cappa, B.M. Messer, W.S. Drisdell, R.C. Cohen, R.J. Saykally, J. Phys. Chem., B 110 (2006) 20038.
[54] R.L.C. Wang, H.J. Kreuzer, M. Grunze, Phys. Chem. Chem. Phys. 8 (2006) 4744.
[55] G. Brancato, N. Rega, V. Barone, Phys. Rev. Lett. 100 (2008) 107401.
[56] C.D. Cappa, J.D. Smith, K.R. Wilson, R.J. Saykally, J. Phys.: Condens. Matter 20 (2008) 205105.
[57] C.T. Chantler, J. Phys. Chem. Ref. Data 29 (2000) 597.
[58] M. Nagasaka, H. Yuzawa, N. Kosugi, UVSOR Activity Report 2013, 2014, pp. 110.
[59] M. Nagasaka, H. Yuzawa, N. Kosugi, UVSOR Activity Report 2013, 2014, pp. 112.
[60] H. Yuzawa, M. Nagasaka, N. Kosugi, J. Phys. Chem., C 119 (2015) 7738.
[61] M. Nagasaka, H. Yuzawa, T. Horigome, A.P. Hitchcock, N. Kosugi, J. Phys. Chem., C 117 (2013) 16343.
[62] M. Nagasaka, H. Yuzawa, T. Horigome, N. Kosugi, Rev. Sci. Instrum. 85 (2014) 104105.
[63] T. Hatsui, E. Shigemasa, N. Kosugi, AIP Conf. Proc. 705 (2004) 921.
[64] R. Flesch, A.A. Pavlychev, J.J. Neville, J. Blumberg, M. Kuhlmann, W. Tappe, F. Senf, O. Schwarzkopf, A.P. Hitchcock, E. Rühl, Phys. Rev. Lett. 86 (2001) 3767.
[65] M. Coreno, M. de Simone, K.C. Prince, R. Richter, M. Vondráček, L. Avaldi, R. Camilloni, Chem. Phys. Lett. 306 (1999) 269.
[66] M. Yamagami, T. Yamaguchi, H. Wakita, M. Misawa, J. Chem. Phys. 100 (1994) 3122.
[67] R. Leberman, A.K. Soper, Nature 378 (1995) 364.
[68] A.K. Soper, K. Weckström, Biophys. Chem. 124 (2006) 180.
[69] S. Bouazizi, F. Hammami, S. Nasr, M.-C. Bellissent-Funel, J. Mol. Struct. 892 (2008) 47.
[70] S. Bouazizi, S. Nasr, N. Jaîdane, M.-C. Bellissent-Funel, J. Phys. Chem., B 110 (2006) 23515.
[71] S. Bouazizi, S. Nasr, J. Mol. Struct. 837 (2007) 206.
[72] S. Bouazizi, S. Nasr, J. Mol. Struct. 875 (2008) 121.
[73] J. Mähler, I. Persson, Inorg. Chem. 51 (2012) 425.
[74] V.A. Glezakou, Y.S. Chen, J.L. Fulton, G.K. Schenter, L.X. Dang, Theor. Chem. Acc. 115 (2006) 86.
[75] T. Megyes, S. Bálint, T. Grósz, T. Radnai, I. Bakó, P. Sipos, J. Chem. Phys. 128 (2008) 044501.
[76] B. Winter, R. Weber, I.V. Hertel, M. Faubel, P. Jungwirth, E.C. Brown, S.E. Bradforth, J. Am. Chem. Soc. 127 (2005) 7203.
[77] Z. Yin, I. Rajkovic, K. Kubicek, W. Quevedo, A. Pietzsch, P. Wernet, A. Föhlisch, S. Techert, J. Phys. Chem., B 118 (2014) 9398.
[78] G. Tóth, J. Chem. Phys. 105 (1996) 5518.
[79] A. Tongraar, K.R. Liedl, B.M. Rode, Chem. Phys. Lett. 286 (1998) 56.
[80] J.A. White, E. Schwegler, G. Galli, F. Gygi, J. Chem. Phys. 113 (2000) 4668.
[81] A.V. Egorov, A.V. Komolkin, V.I. Chizhik, P.V. Yushmanov, A.P. Lyubartsev, A. Laaksonen, J. Phys. Chem., B 107 (2003) 3234.
[82] D. Spångberg, K. Hermansson, J. Chem. Phys. 120 (2004) 4829.
[83] S. Chowdhuri, A. Chandra, J. Phys. Chem., B 110 (2006) 9674.
[84] E. Guàrdia, D. Laria, J. Martí, J. Phys. Chem., B 110 (2006) 6332.
[85] A.S. Thomas, A.H. Elcock, J. Am. Chem. Soc. 129 (2007) 14887.
[86] Y. Liu, H. Lu, Y. Wu, T. Hu, Q. Li, J. Chem. Phys. 132 (2010) 124503.
[87] A. Bankura, V. Carnevale, M.L. Klein, J. Chem. Phys. 138 (2013) 014501.
[88] N. Galamba, J. Phys. Chem., B 117 (2013) 589.
[89] P. Sripa, A. Tongraar, T. Kerdcharoen, J. Phys. Chem., A 117 (2013) 1826.
[90] A.P. Gaiduk, C. Zhang, F. Gygi, G. Galli, Chem. Phys. Lett. 604 (2014) 89.
[91] J.J. Xu, H.B. Yi, H.J. Li, Y. Chen, Mol. Phys. 112 (2014) 1710.
[92] E.F. Aziz, A. Zimina, M. Freiwald, S. Eisebitt, W. Eberhardt, J. Chem. Phys. 124 (2006) 114502.
[93] W. Wachter, Š. Fernandez, R. Buchner, G. Hefter, J. Phys. Chem., B 111 (2007) 9010.
[94] M.F. Kropman, H.J. Bakker, Science 291 (2001) 2118.
[95] M.F. Kropman, H.J. Bakker, J. Chem. Phys. 115 (2001) 8942.
[96] A.W. Omta, M.F. Kropman, S. Woutersen, H.J. Bakker, Science 301 (2003) 347.
[97] A.W. Omta, M.F. Kropman, S. Woutersen, H.J. Bakker, J. Chem. Phys. 119 (2003) 12457.
[98] A.K. Soper, Chem. Phys. 258 (2000) 121.
[99] K. Modig, B.G. Pfrommer, B. Halle, Phys. Rev. Lett. 90 (2003) 075502.
[100] M. Hakala, K. Nygård, S. Manninen, L.G.M. Pettersson, K. Hämäläinen, Phys. Rev. B: Condens. Matter 73 (2006) 035432.
[101] K. Nygård, M. Hakala, T. Pylkkänen, S. Manninen, T. Buslaps, M. Itou, A. Andrejczuk, Y. Sakurai, M. Odelius, K. Hämäläinen, J. Chem. Phys. 126 (2007) 154508.
[102] J.D. Smith, C.D. Cappa, K.R. Wilson, R.C. Cohen, P.L. Geissler, R.J. Saykally, Proc. Natl. Acad. Sci. U.S.A. 102 (2005) 14171.
[103] B.M. Auer, J.L. Skinner, J. Chem. Phys. 128 (2008) 224511.
[104] D. Kraemer, M.L. Cowan, A. Paarmann, N. Huse, E.T.J. Nibbering, T. Elsaesser, R.J.D. Miller, Proc. Natl. Acad. Sci. U.S.A. 105 (2008) 437.
[105] M. Paolantoni, N.F. Lago, M. Albertí, A. Laganà, J. Phys. Chem., A 113 (2009) 15100.
[106] J.R. Errington, P.G. Debenedetti, Nature 409 (2001) 318.
[107] Z. Yan, S.V. Buldyrev, P. Kumar, N. Giovambattista, P.G. Debenedetti, H.E. Stanley, Phys. Rev. E: Stat. Nonlinear Soft Matter 76 (2007) 051201.
[108] M. Magini, G. Paschina, G. Piccaluga, J. Chem. Phys. 77 (1982) 2051.
[109] A.H. Narten, A. Habenschuss, J. Chem. Phys. 80 (1984) 3387.
[110] Y. Tanaka, N. Ohtomo, K. Arakawa, Bull. Chem. Soc. Jpn. 57 (1984) 644.
[111] Y. Tanaka, N. Ohtomo, K. Arakawa, Bull. Chem. Soc. Jpn. 58 (1985) 270.
[112] S. Sarkar, R.N. Joarder, J. Chem. Phys. 99 (1993) 2032.
[113] T. Yamaguchi, K. Hidaka, A.K. Soper, Mol. Phys. 96 (1999) 1159.
[114] R. Ludwig, Angew. Chem. Int. Ed. 40 (2001) 1808.
[115] A.K. Soper, J.L. Finney, Phys. Rev. Lett. 71 (1993) 4346.
[116] L. Dougan, S.P. Bates, R. Hargreaves, J.P. Fox, J. Crain, J.L. Finney, V. Réat, A.K. Soper, J. Chem. Phys. 121 (2004) 6456.
[117] C. Corsaro, J. Spooren, C. Branca, N. Leone, M. Broccio, C. Kim, S. Chen, H.E. Stanley, F. Mallamace, J. Phys. Chem., B 112 (2008) 10449.
[118] T. Takamuku, T. Yamaguchi, M. Asato, M. Matsumoto, N. Nishi, Z. Naturforsch. 55 (2000) 513.
[119] N. Micali, S. Trusso, C. Vasi, D. Blaudez, F. Mallamace, Phys. Rev. E: Stat. Nonlinear Soft Matter 54 (1996) 1720.
[120] T. Sato, A. Chiba, R. Nozaki, J. Chem. Phys. 112 (2000) 2924.
[121] M. Falk, E. Whalley, J. Chem. Phys. 34 (1961) 1554.
[122] W.F. Passchier, E.R. Klompmaker, M. Mandel, Chem. Phys. Lett. 4 (1970) 485.
[123] J.E. Bertie, S.L. Zhang, H.H. Eysel, S. Baluja, M.K. Ahmed, Appl. Spectrosc. 47 (1993) 1100.
[124] D.S. Venables, C.A. Schmuttenmaer, J. Chem. Phys. 113 (2000) 11222.
[125] D. Adachi, Y. Katsumoto, H. Sato, Y. Ozaki, Appl. Spectrosc. 56 (2002) 357.
[126] G. Ma, H.C. Allen, J. Phys. Chem., B 107 (2003) 6343.
[127] K.N. Woods, H. Wiedemann, J. Chem. Phys. 123 (2005) 134507.
[128] M.K. Ahmed, S. Ali, E. Wojcik, Spectr. Lett. 45 (2012) 420.
[129] G. Kabisch, K. Pollmer, J. Mol. Struct. 81 (1982) 35.
[130] M. Schwartz, A. Moradi-Araghi, W.H. Koehler, J. Mol. Struct. 81 (1982) 245.
[131] K. Lin, X. Zhou, Y. Luo, S. Liu, J. Phys. Chem., B 114 (2010) 3567.
[132] M. Haughney, M. Ferrario, I.R. McDonald, J. Phys. Chem. 91 (1987) 4934.
[133] M. Ferrario, M. Haughney, I.R. McDonald, M.L. Klein, J. Chem. Phys. 93 (1990) 5156.
[134] M.S. Skaf, B.M. Ladanyi, J. Phys. Chem. 100 (1996) 18258.
[135] A. Laaksonen, P.G. Kusalik, I.M. Svishchev, J. Phys. Chem., A 101 (1997) 5910.
[136] E. Tsuchida, Y. Kanada, M. Tsukada, Chem. Phys. Lett. 311 (1999) 236.
[137] T.S. van Erp, E.J. Meijer, Chem. Phys. Lett. 333 (2001) 290.
[138] J.A. Morrone, M.E. Tuckerman, J. Chem. Phys. 117 (2002) 4403.
[139] M. Pagliai, G. Cardini, R. Righini, V. Schettino, J. Chem. Phys. 119 (2003) 6655.
[140] J.-W. Handgraaf, E.J. Meijer, M.-P. Gaigeot, J. Chem. Phys. 121 (2004) 10111.
[141] H. Yu, D.P. Geerke, H. Liu, W.F. Van Gunsteren, J. Comput. Chem. 27 (2006) 1494.
[142] Y. Zhong, G.L. Warren, S. Patel, J. Comput. Chem. 29 (2007) 1142.
[143] I. Bakó, T. Megyes, S. Bálint, T. Grósz, V. Chihaia, Phys. Chem. Chem. Phys. 10 (2008) 5004.
[144] P.L. Silvestrelli, J. Phys. Chem., B 113 (2009) 10728.
[145] T. Ishiyama, V.V. Sokolov, A. Morita, J. Chem. Phys. 134 (2011) 024509.
[146] S.T. Moin, T.S. Hofer, B.R. Randolf, B.M. Rode, J. Comput. Chem. 32 (2011) 886.
[147] W.L. Jorgensen, J. Am. Chem. Soc. 102 (1980) 543.
[148] S. Okazaki, H. Touhara, K. Nakanishi, J. Chem. Phys. 81 (1984) 890.
[149] I. Adamovic, M.S. Gordon, J. Phys. Chem., A 110 (2006) 10267.

[150] M. Valdéz-González, H. Saint-Martin, J. Hernández-Cobos, J. Chem. Phys. 127 (2007) 224507.
[151] J.A.B. da Silva, F.G.B. Moreira, V.M.L. dos Santos, R.L. Longo, Phys. Chem. Chem. Phys. 13 (2011) 6452.
[152] J.A.B. da Silva, F.G.B. Moreira, V.M.L. dos Santos, R.L. Longo, Phys. Chem. Chem. Phys. 13 (2011) 593.
[153] J.-H. Guo, Y. Luo, A. Augustsson, S. Kashtanov, J.-E. Rubensson, D.K. Shuh, H. Ågren, J. Nordgren, Phys. Rev. Lett. 91 (2003) 157401.
[154] S. Kashtanov, A. Augustsson, J.-E. Rubensson, J. Nordgren, H. Ågren, J.-H. Guo, Y. Luo, Phys. Rev. B: Condens. Matter 71 (2005) 104205.
[155] A. Hempelmann, M.N. Piancastelli, F. Heiser, O. Gessner, A. Rüdel, U. Becker, J. Phys., B: At. Mol. Opt. Phys. 32 (1999) 2677.
[156] K.C. Prince, R. Richter, M. de Simone, M. Alagia, M. Coreno, J. Phys. Chem., A 107 (2003) 1955.
[157] B. Hess, C. Kutzner, D. van der Spoel, E. Lindahl, J. Chem. Theory Comput. 4 (2008) 435.
[158] W.L. Jorgensen, J. Tirado-Rives, Proc. Natl. Acad. Sci. U.S.A. 102 (2005) 6665.
[159] C. Caleman, P.J. Van Maaren, M. Hong, J.S. Hub, L.T. Costa, D. Van der Spoel, J. Chem. Theory Comput. 8 (2012) 61.
[160] M.W. Mahoney, W.L. Jorgensen, J. Chem. Phys. 112 (2000) 8910.
[161] S. Nose, J. Phys.: Condes. Matter 2 (1990) SA115.
[162] M. Parrinello, A. Rahman, J. Appl. Phys. 52 (1981) 7182.
[163] T. Darden, D. York, L. Pedersen, J. Chem. Phys. 98 (1993) 10089.
[164] A. Dkhissi, L. Adamowicz, G. Maes, J. Phys. Chem., A 104 (2000) 2112.
[165] I. Pápai, G. Jancsó, J. Phys. Chem., A 104 (2000) 2132.
[166] T. Malaspina, K. Coutinho, S. Canuto, J. Chem. Phys. 117 (2002) 1692.
[167] H. Arai, Y. Horikawa, K. Sadakane, T. Tokushima, Y. Harada, Y. Senba, H. Ohashi, Y. Takata, S. Shin, Phys. Chem. Chem. Phys. 14 (2012) 1576.
[168] T. Tokushima, Y. Horikawa, O. Takahashi, H. Arai, K. Sadakane, Y. Harada, Y. Takata, S. Shin, Phys. Chem. Chem. Phys. 16 (2014) 10753.
[169] M. Nagasaka, T. Hatsui, N. Kosugi, J. Electron. Spectrosc. Relat. Phenom. 166–167 (2008) 16.
[170] M. Nagasaka, T. Hatsui, H. Setoyama, E. Rühl, N. Kosugi, J. Electron. Spectrosc. Relat. Phenom. 183 (2011) 29.
[171] M. Piacenza, S. Grimme, ChemPhysChem 6 (2005) 1554.
[172] H. Kovacs, A. Laaksonen, J. Am. Chem. Soc. 113 (1991) 5596.
[173] D.L. Bergman, A. Laaksonen, Phys. Rev. E: Stat. Nonlinear Soft Matter 58 (1998) 4706.
[174] C. Oldiges, K. Wittler, T. Tönsing, A. Alijah, J. Phys. Chem., A 106 (2002) 7147.
[175] I. Bakó, T. Megyes, G. Pálinkás, Chem. Phys. 316 (2005) 235.
[176] K.M. Lange, K.F. Hodeck, U. Schade, E.F. Aziz, J. Phys. Chem., B 114 (2010) 16997.
[177] N. Huang, D. Nordlund, C. Huang, U. Bergmann, T.M. Weiss, L.G.M. Pettersson, A. Nilsson, J. Chem. Phys. 135 (2011) 164509.
[178] T. Radnai, S. Itoh, H. Ohtaki, Bull. Chem. Soc. Jpn. 61 (1988) 3845.
[179] C. Moreau, G. Douhéret, J. Chem. Thermodyn. 8 (1976) 403.
[180] T. Takamuku, Y. Noguchi, M. Matsugami, H. Iwase, T. Otomo, M. Nagao, J. Mol. Liq. 136 (2007) 147.
[181] K. Nishikawa, Y. Kasahara, T. Ichioka, J. Phys. Chem., B 106 (2002) 693.
[182] D.N. Shin, J.W. Wijnen, J.B.F.N. Engberts, A. Wakisaka, J. Phys. Chem., B 106 (2002) 6014.
[183] F. Zaera, Surf. Sci. 605 (2011) 1141.
[184] F. Zaera, Chem. Rev. 112 (2012) 2920.
[185] P.J. Ellis, I.J.S. Fairlamb, S.F.J. Hackett, K. Wilson, A.F. Lee, Angew. Chem. Int. Ed. 49 (2010) 1820.
[186] D. Friebel, D.J. Miller, D. Nordlund, H. Ogasawara, A. Nilsson, Angew. Chem. Int. Ed. 50 (2011) 10190.
[187] S. Reimann, J. Stotzel, R. Frahm, W. Kleist, J.D. Grunwaldt, A. Baiker, J. Am. Chem. Soc. 133 (2011) 3921.
[188] A.M. Karim, C. Howard, B. Roberts, L. Kovarik, L. Zhang, D.L. King, Y. Wang, ACS Catal. 2 (2012) 2387.
[189] V. Belliere, C. Lorentz, C. Geantet, Y. Yoshimura, D. Laurenti, M. Vrinat, Appl. Catal., B: Environ. 64 (2006) 254.
[190] J. Huang, W. Long, P.K. Agrawal, C.W. Jones, J. Phys. Chem., C 113 (2009) 16702.
[191] A. Vjunov, M.Y. Hu, J. Feng, D.M. Camaioni, D.H. Mei, J.Z. Hu, C. Zhao, J.A. Lercher, Angew. Chem. Int. Ed. 53 (2014) 479.
[192] T. Burgi, A. Baiker, J. Phys. Chem., B 106 (2002) 10649.
[193] D. Ferri, S. Diezi, M. Maciejewski, A. Baiker, Appl. Catal., A: Gen. 297 (2006) 165.
[194] D. Ferri, A. Baiker, Top. Catal. 52 (2009) 1323.
[195] J.M. Andanson, A. Baiker, Chem. Soc. Rev. 39 (2010) 4571.
[196] A. Aguirre, A.L. Bonivardi, S.R. Matkovic, L.E. Briand, S.E. Collins, Top. Catal. 54 (2011) 229.
[197] P. Leinweber, J. Kruse, F.L. Walley, A. Gillespie, K.U. Eckhardt, R.I.R. Blyth, T. Regier, J. Synchrot. Radiat. 14 (2007) 500.
[198] A.L. Marsh, D.J. Burnett, D.A. Fischer, J.L. Gland, J. Phys. Chem., B 107 (2003) 12472.
[199] S.D. Senanayake, D. Stacchiola, J. Evans, M. Estrella, L. Barrio, M. Perez, J. Hrbek, J.A. Rodriguez, J. Catal. 271 (2010) 392.
[200] F. Morales, F.M.F. de Groot, P. Glatzel, E. Kleimenov, H. Bluhm, M. Havecker, A. Knop-Gericke, B.M. Weckhuysen, J. Phys. Chem., B 108 (2004) 16201.
[201] S. Aminpirooz, L. Becker, B. Hillert, J. Haase, Surf. Sci. 244 (1991) L152.
[202] G. Vall-llosera, B. Gao, A. Kivimäki, M. Coreno, J. Álvarez Ruiz, M. de Simone, H. Ågren, E. Rachlew, J. Chem. Phys. 128 (2008) 044316.
[203] A.P. Hitchcock, M. Tronc, A. Modelli, J. Phys. Chem. 93 (1989) 3068.
[204] K. Sugiyama, H. Miura, Y. Nakano, H. Sekiwa, T. Matsuda, Bull. Chem. Soc. Jpn. 59 (1986) 2983.
[205] K. Yamaguchi, M. Matsushita, N. Mizuno, Angew. Chem. Int. Ed. 43 (2004) 1576.
[206] S.C. Roy, P. Dutta, L.N. Nandy, S.K. Roy, P. Samuel, S.M. Pillai, V.K. Kaushik, M. Ravindranathan, Appl. Catal., A: Gen. 290 (2005) 175.
[207] M. Tamura, H. Wakasugi, K. Shimizu, A. Satsuma, Chem. Eur. J. 17 (2011) 11428.
[208] M. Tamura, A. Satsuma, K. Shimizu, Catal. Sci. Technol. 3 (2013) 1386.
[209] K. Ashley, S. Pons, Chem. Rev. 88 (1988) 673.
[210] M. Nakamura, H. Kato, N. Hoshi, J. Phys. Chem., C 112 (2008) 9458.
[211] S. Nihonyanagi, S. Ye, K. Uosaki, L. Dreesen, C. Humbert, P. Thiry, A. Peremans, Surf. Sci. 573 (2004) 11.
[212] B. Pettinger, M.R. Philpott, J.G. Gordon II, Surf. Sci. 105 (1981) 469.
[213] K. Ataka, T. Yotsuyanagi, M. Osawa, J. Phys. Chem. 100 (1996) 10664.
[214] M.F. Toney, J.N. Howard, J. Richer, G.L. Borges, J.G. Gordon, O.R. Melroy, D.G. Wiesler, D. Yee, L.B. Sorensen, Nature 368 (1994) 444.
[215] N. De Jonge, F.M. Ross, Nat. Nanotechnol. 6 (2011) 695.
[216] S. Wu, J. Lipkowski, T. Tyliszczak, A.P. Hitchcock, Prog. Surf. Sci. 50 (1995) 227.
[217] S. Wu, Z. Shi, J. Lipkowski, A.P. Hitchcock, T. Tyliszczak, J. Phys. Chem., B 101 (1997) 10310.
[218] O. Endo, M. Kiguchi, T. Yokoyama, M. Ito, T. Ohta, J. Electroanal. Chem. 473 (1999) 19.
[219] I. Nakai, Y. Shiraishi, F. Nishikawa, Spectroc. Acta, B 54 (1999) 143.
[220] D.K. Bediako, B. Lassalle-Kaiser, Y. Surendranath, J. Yano, V.K. Yachandra, D.G. Nocera, J. Am. Chem. Soc. 134 (2012) 6801.
[221] T. Masuda, H. Yoshikawa, H. Noguchi, T. Kawasaki, M. Kobata, K. Kobayashi, K. Uosaki, Appl. Phys. Lett. 103 (2013) 111605.
[222] D.K. Bora, P.-A. Glans, J. Pepper, Y.-S. Liu, C. Du, D. Wang, J.-H. Guo, Rev. Sci. Instrum. 85 (2014) 043106.
[223] C. Schwanke, R. Golnak, J. Xiao, K.M. Lange, Rev. Sci. Instrum. 85 (2014) 103120.
[224] D. Guay, J. Stewart-Ornstein, X. Zhang, A.P. Hitchcock, Anal. Chem. 77 (2005) 3479.
[225] B. Bozzini, L. D'Urzo, A. Gianoncelli, B. Kaulich, M. Prasciolu, I. Sgura, E. Tondo, M. Kiskinova, J. Phys. Chem. C 113 (2009) 9783.
[226] B. Bozzini, A. Gianoncelli, P. Bocchetta, S. Dal Zilio, G. Kourousias, Anal. Chem. 86 (2014) 664.
[227] A.F. Gil, L. Galicia, I. González, J. Electroanal. Chem. 417 (1996) 129.
[228] R.E. Huffman, N. Davidson, J. Am. Chem. Soc. 78 (1956) 4836.
[229] J. Beukenkamp, K.D. Herrington, J. Am. Chem. Soc. 82 (1960) 3022.
[230] M. Iwai, H. Majima, Y. Awakura, Metall. Mater. Trans., B 13 (1982) 311.
[231] A.F. Gil, L. Salgado, L. Galicia, I. González, Talanta 42 (1995) 407.
[232] K. Kunimatsu, H. Hanawa, H. Uchida, M. Watanabe, J. Electroanal. Chem. 632 (2009) 109.
[233] J. Wang, B.M. Ocko, A.J. Davenport, H.S. Isaacs, Phys. Rev. B: Condens. Matter 46 (1992) 10321.
[234] M. Nakamura, O. Endo, T. Ohta, M. Ito, Y. Yoda, Surf. Sci. 514 (2002) 227.
[235] B. Braunschweig, P. Mukherjee, D.D. Dlott, A. Wieckowski, J. Am. Chem. Soc. 132 (2010) 14036.
[236] N. Huse, T.K. Kim, L. Jamula, J.K. McCusker, F.M.F. de Groot, R.W. Schoenlein, J. Am. Chem. Soc. 132 (2010) 6809.
[237] Y. Obara, T. Katayama, Y. Ogi, T. Suzuki, N. Kurahashi, S. Karashima, Y. Chiba, Y. Isokawa, T. Togashi, Y. Inubushi, M. Yabashi, T. Suzuki, K. Misawa, Opt. Exp. 22 (2014) 1105.
[238] T. Warwick, K. Franck, J.B. Kortright, G. Meigs, M. Moronne, S. Myneni, E. Rotenberg, S. Seal, W.F. Steele, H. Ade, A. Garcia, S. Cerasari, J. Delinger, S. Hayakawa, A.P. Hitchcock, T. Tyliszczak, J. Kikuma, E.G. Rightor, H.J. Shin, B.P. Tonner, Rev. Sci. Instrum. 69 (1998) 2964.
[239] T. Ohigashi, H. Arai, T. Araki, N. Kondo, E. Shigemasa, A. Ito, N. Kosugi, M. Katoh, J. Phys.: Conf. Ser. 463 (2013) 012006.